Acta Numerica (2004), pp. 371–431
DOI: 10.1017/S0962492904000200

Multiscale computational modelling of the heart

N. P. Smith, D. P. Nickerson, E. J. Crampin and P. J. Hunter*
Bioengineering Institute,
The University of Auckland,
Private Bag 92019 Auckland,
New Zealand
E-mail: p.hunter@auckland.ac.nz

A computational framework is presented for integrating the electrical, mechanical and biochemical functions of the heart. Finite element techniques are used to solve the large-deformation soft tissue mechanics using orthotropic constitutive laws based in the measured fibre-sheet structure of myocardial (heart muscle) tissue. The reaction–diffusion equations governing electrical current flow in the heart are solved on a grid of deforming material points which access systems of ODEs representing the cellular processes underlying the cardiac action potential. Navier–Stokes equations are solved for coronary blood flow in a system of branching blood vessels embedded in the deforming myocardium and the delivery of oxygen and metabolites is coupled to the energy-dependent cellular processes. The framework presented here for modelling coupled physical conservation laws at the tissue and organ levels is also appropriate for other organ systems in the body and we briefly discuss applications to the lungs and the musculo-skeletal system. The computational framework is also designed to reach down to subcellular processes, including signal transduction cascades and metabolic pathways as well as ion channel electrophysiology, and we discuss the development of ontologies and markup language standards that will help link the tissue and organ level models to the vast array of gene and protein data that are now available in web-accessible databases.

* Supported by grants from the NZ Royal Society (to the Centre for Molecular Biodiscovery and the New Zealand Institute of Mathematics and its Applications) and the NZ Foundation for Research Science and Technology.

CONTENTS

1 Introduction 372
2 Finite element modelling of cardiac tissue 374
3 Continuum modelling 384
4 Cellular modelling 399
5 Vascular blood flow 412
6 Future directions 421
7 Conclusion 425
References 426

1. Introduction

The application of numerical and computational techniques to interpret, simulate and ultimately elucidate the physiological function of complex whole organ systems has developed rapidly within the last two decades. This has been due partly to the availability of new experimental data at the cell, tissue and organ levels and partly to the improvement in computational algorithms and the parallel increase in availability of high performance computing resources.

Understanding the integrative function of an organ requires the modelling of biological processes at multiple spatial and temporal scales. Efficient contraction of the myocardium (heart muscle) to pump blood from the ventricles depends crucially on the organization of structural proteins at the tissue level and the operation of contractile proteins at the subcellular level. At all levels these processes are nonlinear and time-dependent.

In this review we analyse the mechanical, electrical and biochemical function of the heart using models which are based on the anatomy and biophysics of the cells, tissues and organ. The framework developed here for the heart is, however, applicable to all organ systems of the body and we briefly illustrate its application to the lungs and musculo-skeletal system at the end of the article.

1.1. Anatomy and physiology of the heart

The heart is a four-chambered pump with two priming chambers, the left and right atria, and two primary pumping chambers, the left and right ventricles (LV and RV, respectively). Blood is pumped from the RV via the pulmonary artery to the lungs at a peak pressure of about 4 kPa and from the LV via the aorta to the rest of the body at a peak pressure of about 17 kPa. Blood is ejected from the ventricles by the contraction of the myocardium when triggered by changes in the electrical potential across the muscle cell

(myocyte) outer membrane (sarcolemma). The electrical potential inside the myocytes is normally maintained at −85 mV relative to the extracellular fluid. Electric current flow into a cell (inward current) raises the potential (depolarizes the cell) and initiates wave propagation along the electrically conducting cells which are also electrically connected by gap junction proteins. These electrically connected cells act as a cable but with continual regeneration of the signal via inward current through voltage-sensitive ion channels (see later). The whole electrical activation process is initiated under normal physiological conditions by the heart's pacemaker cells, which reside in the right atrium and are called the sino-atrial (SA) node. The signal spontaneously generated by the SA node propagates through the atrial muscle and then to the ventricles via a specialized conducting region (the atrio-ventricular node or AV node). From here the electrical wave travels down specialized conducting fibres called the bundle of His to a network of Purkinje fibres, which spread out through the inner region of the ventricular walls (the endocardium) and make an electrical connection with the myocytes and begin the propagating wavefront that rapidly spreads throughout the myocardium. The entire myocardium is normally activated within 50 ms and the mechanical contraction lasts a further 200–300 ms.

Myocardial tissue has been shown in a number of microstructural studies to consist of layers of interconnected sheets of tissue separated by cleavage planes (Le Grice *et al.* 1995, Nielsen *et al.* 1991). The layers of cells within a sheet are bound tightly together (3 to 4 cells thick) by endomysial collagen (see Figure 1.1). The cells are roughly cylindrical, about 20 μm in diameter, and about 100 μm long. The long axis of the myocytes is called the fibre axis and this varies by up to 150° across the wall, as illustrated in Figure 1.1. The direction orthogonal to the fibres within a sheet is called the sheet axis and the direction orthogonal to the sheet is referred to as the sheet normal. The mechanical and electrical properties of myocardial tissue are orthotropic with these microstructurally based fibre, sheet and sheet-normal axes forming the local material axes to which the constitutive laws are referred (see later). Microstructural detail is critical to both mechanical and electrical function of biological organs and often varies spatially within an organ. It is necessary, therefore, to characterize anisotropic conductivity and mechanical properties in continuum models.

We begin our analysis of heart function by introducing finite element descriptions of organ geometry and microstructure in Section 2. The continuum-based equations and techniques for their solution are outlined in Section 3. Cellular models and their spatial–temporal coupling into the continuum framework are covered in Section 4. Coronary blood flow (blood supply to heart muscle) is considered in Section 5. Finally the challenges and scope for extending this framework and application to other organs are considered in Sections 6 and 7.

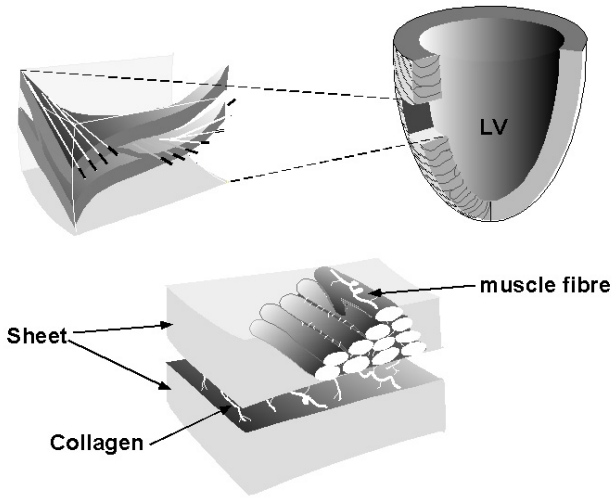

Figure 1.1. Microstructural organization of cardiac tissue. A transmural segment of tissue removed from the left ventricular wall in the upper figure contains muscle fibres that vary in orientation by about 150° (shown by the white lines). These fibres (muscle cells or 'myocytes') are bound tightly together in sheets 3 or 4 cells thick (see lower figure), that are loosely coupled to facilitate mechanical shearing. From Le Grice *et al.* (1995), with permission.

2. Finite element modelling of cardiac tissue

The development of anatomically based representations of organ geometry and tissue properties is the essential first step in the construction of an integrated model of whole organ function. In the following section a finite element method for representation of these fields is introduced. In Section 2.2 methods for determining nodal parameter values used in finite element interpolation functions are outlined.

2.1. Representation of fields

The finite element method is one of the most commonly used approaches to numerically represent spatially distributed fields. Traditionally, finite element models use low-order Lagrangian interpolation and, with very few exceptions, only one type of interpolation scheme in the solution domain. For a detailed introduction to the finite element method readers are referred to Zienkiewicz and Taylor (1994). In this review we present a different approach which uses high-order Hermitian interpolation to provide improved

efficiency and convergence properties (Hunter 1975, Bradley, Pullan and Hunter 1997) for representing the nonlinear and C^1-continuous variation typical of many biological fields.

In the notation used below, ξ_i is the local finite element coordinate in the ith direction ($0 \leq \xi_i \leq 1$), u represents the field variable and u_n its value at local node n of a given element. $\Delta(n, e)$ maps the local node n of element e to its unique global number for a particular mesh. Continuity of the derivative of u with respect to ξ_i across element boundaries is achieved by defining additional nodal parameters which are the partial derivatives of the field variable u with respect to the local coordinate $\left(\frac{\partial u}{\partial \xi_i}\right)_n$. Illustrating this concept in one dimension, basis functions are chosen to ensure that nodal derivatives which contribute to the interpolation within an element are shared by two adjacent elements in order to maintain derivative continuity across different boundaries. Derivative continuity requires cubic interpolation and therefore four-element parameters. These parameters are specified as the nodal value and its derivative with respect to ξ for two nodes per element in one dimension. Thus:

$$u(\xi) = a + b\xi + c\xi^2 + d\xi^3, \quad \text{and therefore} \quad \frac{\mathrm{d}u}{\mathrm{d}\xi} = b + 2c\xi + 3d\xi^2,$$

where

$$a = u_1, \quad b = u'_1, \quad c = 3u_2 - 3u_1 - 2u'_1 - u'_2, \quad d = u'_1 + u'_2 + 2u_1 - 2u_2,$$

or, rearranging,

$$u(\xi) = H_1^0(\xi)u_1 + H_1^1(\xi)u'_1 + H_2^0(\xi)u_2 + H_2^1(\xi)u'_2 \tag{2.1}$$

where $u'_n = \left(\frac{\mathrm{d}u}{\mathrm{d}\xi}\right)_n$, and the four one-dimensional cubic-Hermite basis functions are illustrated in Figure 2.1.

To constrain continuity across element boundaries in the global coordinate system, rather than in the local ξ coordinate system, a further modification is required. The derivative $\left(\frac{\mathrm{d}u}{\mathrm{d}\xi}\right)_n$ defined at node n is dependent upon the element ξ-coordinate in the two adjacent elements. It is more useful to define a global node derivative $\left(\frac{\mathrm{d}u}{\mathrm{d}s}\right)_n$ where s is arclength, and then use

$$\left(\frac{\mathrm{d}u}{\mathrm{d}\xi}\right)_n = \left(\frac{\mathrm{d}u}{\mathrm{d}s}\right)_{\Delta(n,e)} \cdot \left(\frac{\mathrm{d}s}{\mathrm{d}\xi}\right)_n \tag{2.2}$$

where $\left(\frac{\mathrm{d}s}{\mathrm{d}\xi}\right)_n$ is an element 'scale factor' which scales the arclength derivative of global node Δ to the ξ-coordinate derivative of element node n.

Achieving derivative continuity in three dimensions for the element shown in Figure 2.2 requires eight values per node:

$$u, \quad \frac{\partial u}{\partial \xi_1}, \quad \frac{\partial u}{\partial \xi_2}, \quad \frac{\partial u}{\partial \xi_3}, \quad \text{and} \quad \frac{\partial^2 u}{\partial \xi_1 \partial \xi_2}, \quad \frac{\partial^2 u}{\partial \xi_1 \partial \xi_3}, \quad \frac{\partial^2 u}{\partial \xi_2 \partial \xi_3}, \quad \frac{\partial^3 u}{\partial \xi_1 \partial \xi_2 \partial \xi_3}.$$

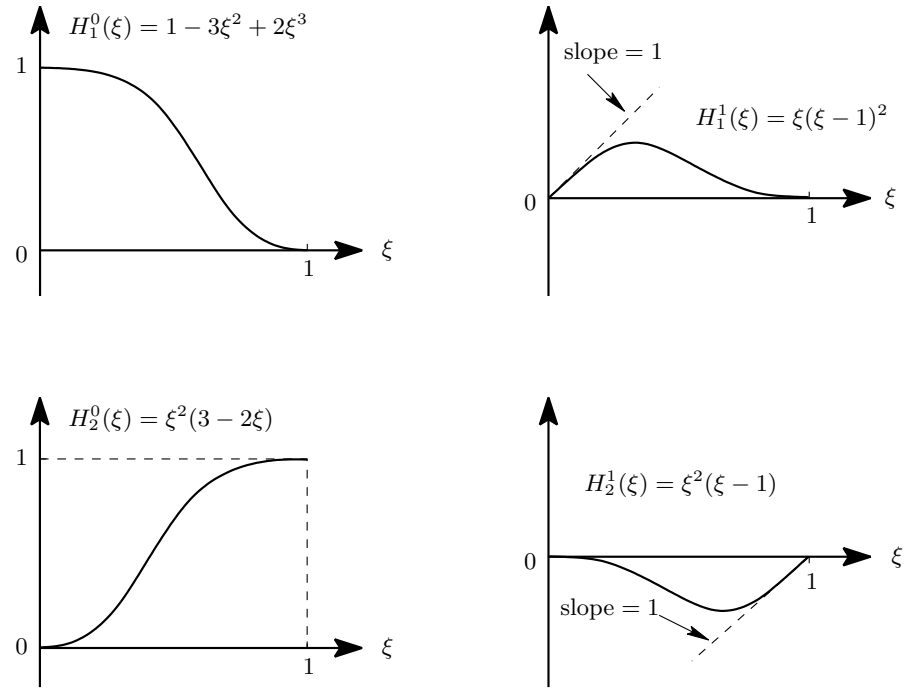

Figure 2.1. Cubic-Hermite basis functions.

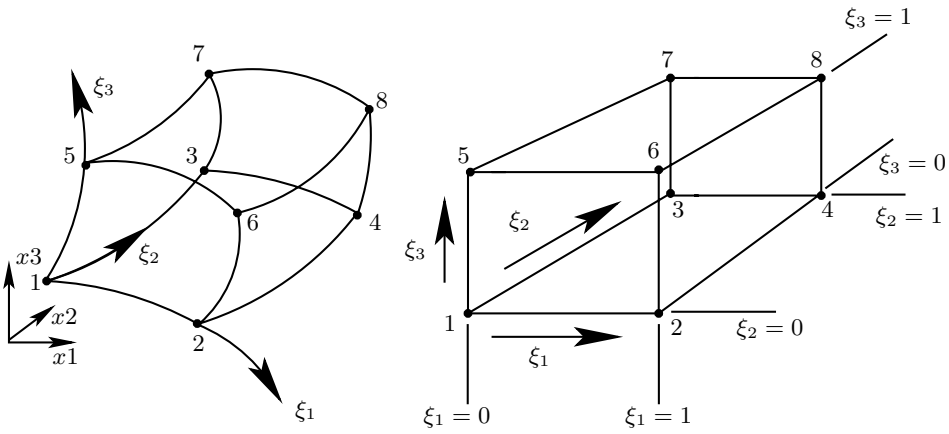

Figure 2.2. Schematic and local node numbering of a 3D element shown in physical space on the left and transformed into ξ space on the right.

The second-order cross-derivative terms arise from the need to maintain cubic interpolation along every element edge in each ξ direction. To illustrate, we consider a particular edge of a three-dimensional element where moving between nodes corresponds to only increasing in ξ_1. The cubic variation in u can be uniquely specified by u and $\frac{\partial u}{\partial \xi_1}$ at each node. However, $\frac{\partial u}{\partial \xi_2}$, $\frac{\partial u}{\partial \xi_3}$ and $\frac{\partial^2 u}{\partial \xi_2 \partial \xi_3}$ should also vary cubically and are completely independent of these parameters. Thus six additional parameters are specified for each node. Tricubic interpolation of these nodal parameters is given by

$$
\begin{aligned}
&u(\xi_1,\xi_2,\xi_3) = \qquad (2.3)\\
&\sum_{k=1}^{2}\sum_{j=1}^{2}\sum_{i=1}^{2}\Bigg[H_i^0(\xi_1)H_j^0(\xi_2)H_k^0(\xi_3)u_n + H_i^1(\xi_1)H_j^0(\xi_2)H_k^0(\xi_3)\left(\frac{\partial u}{\partial \xi_1}\right)_n +\\
&H_i^0(\xi_1)H_j^1(\xi_2)H_k^0(\xi_3)\left(\frac{\partial u}{\partial \xi_2}\right)_n + H_i^0(\xi_1)H_j^0(\xi_2)H_k^1(\xi_3)\left(\frac{\partial u}{\partial \xi_3}\right)_n +\\
&H_i^1(\xi_1)H_j^1(\xi_2)H_k^0(\xi_3)\left(\frac{\partial^2 u}{\partial \xi_1 \partial \xi_2}\right)_n + H_i^1(\xi_1)H_j^0(\xi_2)H_k^1(\xi_3)\left(\frac{\partial^2 u}{\partial \xi_1 \partial \xi_3}\right)_n +\\
&H_i^0(\xi_1)H_j^1(\xi_2)H_k^1(\xi_3)\left(\frac{\partial^2 u}{\partial \xi_2 \partial \xi_3}\right)_n + H_i^1(\xi_1)H_j^1(\xi_2)H_k^1(\xi_3)\left(\frac{\partial^3 u}{\partial \xi_1 \partial \xi_2 \partial \xi_3}\right)_n\Bigg]
\end{aligned}
$$

where the nodal index $n = 4(k-1) + 2(j-1) + i$, and

$$
\begin{aligned}
H_1^0(\xi) &= 1 - 3\xi^2 + 2\xi^3, \quad H_1^1(\xi) = \xi(\xi-1)^2, \qquad (2.4)\\
H_2^0(\xi) &= \xi^2(3-2\xi) \quad \text{and} \quad H_2^1(\xi) = \xi^2(\xi-1),
\end{aligned}
$$

as shown in Figure 2.1. To simplify notation, let

$$
u(\xi_1,\xi_2,\xi_3) = \sum_m \psi_m(\boldsymbol{\xi})\bar{u}_m, \qquad (2.5)
$$

where $\bar{u}_m$ represents the vector of nodal values and their derivatives and ψ_m are formed from the products of the one-dimensional basis functions given in equation (2.4), and the summation over m is taken over all these quantities.

As in the one-dimensional case, to preserve derivative continuity in physical x-coordinate space rather than in ξ-coordinate space the global node derivatives need to be specified with respect to physical arclength. There are now three arclengths to consider: s_i, measuring arclength along the ξ_i-coordinate, for $i = 1, 2, 3$. Thus

$$
\begin{aligned}
\left(\frac{\partial u}{\partial \xi_1}\right)_n &= \left(\frac{\partial u}{\partial s_1}\right)_{\Delta(n,e)} \cdot \left(\frac{\mathrm{d}s_1}{\mathrm{d}\xi_1}\right)_n, \qquad (2.6)\\
\left(\frac{\partial u}{\partial \xi_2}\right)_n &= \left(\frac{\partial u}{\partial s_2}\right)_{\Delta(n,e)} \cdot \left(\frac{\mathrm{d}s_2}{\mathrm{d}\xi_2}\right)_n,
\end{aligned}
$$

$$\left(\frac{\partial u}{\partial \xi_3}\right)_n = \left(\frac{\partial u}{\partial s_3}\right)_{\Delta(n,e)} \cdot \left(\frac{\mathrm{d}s_3}{\mathrm{d}\xi_3}\right)_n,$$

$$\left(\frac{\partial^2 u}{\partial \xi_1 \partial \xi_2}\right)_n = \left(\frac{\partial^2 u}{\partial s_1 \partial s_2}\right)_{\Delta(n,e)} \cdot \left(\frac{\mathrm{d}s_1}{\mathrm{d}\xi_1}\right)_n \cdot \left(\frac{\mathrm{d}s_2}{\mathrm{d}\xi_2}\right)_n,$$

$$\left(\frac{\partial^2 u}{\partial \xi_1 \partial \xi_3}\right)_n = \left(\frac{\partial^2 u}{\partial s_1 \partial s_3}\right)_{\Delta(n,e)} \cdot \left(\frac{\mathrm{d}s_1}{\mathrm{d}\xi_1}\right)_n \cdot \left(\frac{\mathrm{d}s_3}{\mathrm{d}\xi_3}\right)_n,$$

$$\left(\frac{\partial^2 u}{\partial \xi_2 \partial \xi_3}\right)_n = \left(\frac{\partial^2 u}{\partial s_2 \partial s_3}\right)_{\Delta(n,e)} \cdot \left(\frac{\mathrm{d}s_2}{\mathrm{d}\xi_2}\right)_n \cdot \left(\frac{\mathrm{d}s_3}{\mathrm{d}\xi_3}\right)_n,$$

$$\left(\frac{\partial^3 u}{\partial \xi_1 \partial \xi_2 \partial \xi_3}\right)_n = \left(\frac{\partial^3 u}{\partial s_1 \partial s_2 \partial s_3}\right)_{\Delta(n,e)} \cdot \left(\frac{\mathrm{d}s_1}{\mathrm{d}\xi_1}\right)_n \cdot \left(\frac{\mathrm{d}s_2}{\mathrm{d}\xi_2}\right)_n \cdot \left(\frac{\mathrm{d}s_3}{\mathrm{d}\xi_3}\right)_n.$$

Equations (2.3)–(2.6) provide a means of interpolating spatially varying fields that are C^1-continuous.

We have used two alternative approaches to modelling the geometry of the heart. One uses the prolate spheroidal coordinate system shown in Figure 2.3 with bicubic-linear interpolation for the λ-coordinate (bicubic-Hermite in the (ξ_1, ξ_2) plane corresponding to the ventricular surfaces and linear in ξ_3 through the wall) and trilinear interpolation for the θ and μ coordinates. The other approach uses rectangular Cartesian coordinates and fully tricubic-Hermite interpolation.

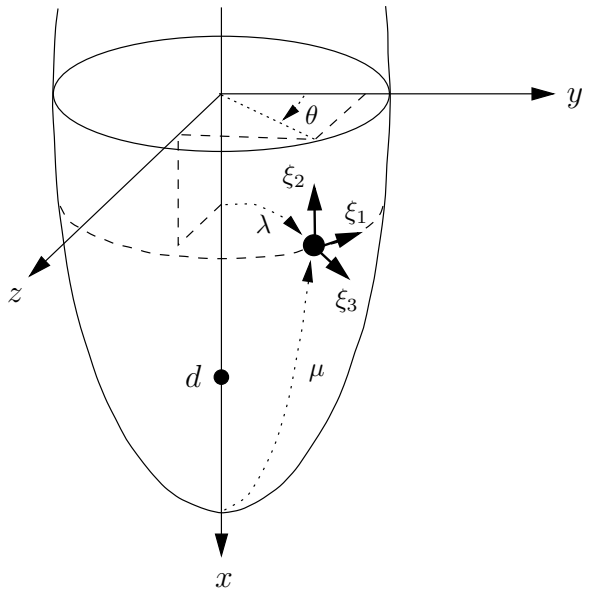

Figure 2.3. The prolate spheroidal and rectangular Cartesian coordinates for the ventricular models shown in Figure 2.4.

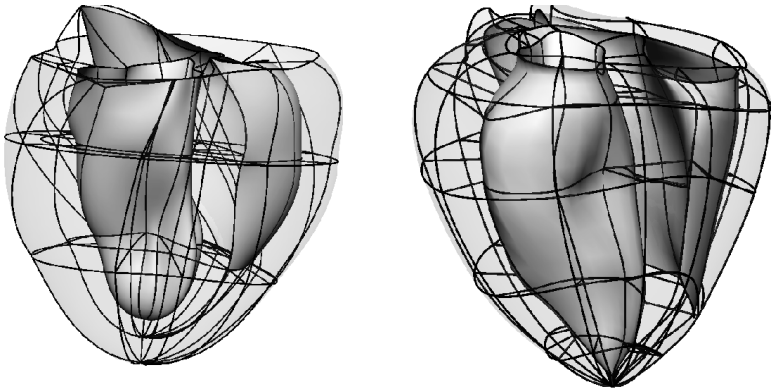

(a) (b)

Figure 2.4. Anatomically accurate canine (a) and porcine (b) finite element models. (a) uses bilinear/cubic-Hermite interpolation based in prolate spheroidal coordinates to represent canine cardiac ventricles, while (b) uses tricubic-Hermite interpolation based in rectangular Cartesian coordinates to represent porcine cardiac ventricles.

As with geometry, cubic-Hermite interpolation can effectively be used to represent the variation in microstructurally based material directions as demonstrated in Figure 2.5, which shows the microstructural field embedded in the geometric models shown in Figure 2.4.

The next step in mesh construction is the calculation of values of variables u_n and their partial derivatives with respect to the local material directions ξ_i at nodes in the finite element mesh. This nonlinear fitting process is outlined in the following section.

2.2. Nonlinear fitting

The geometric fitting algorithm which is used to determine nodal field variables in the finite element tissue models from data is a variant of the well-known Iterative Closest Point (ICP) algorithm, where the surface fit is improved over several iterations. There are a number of implementations of this approach for fitting three-dimensional geometric models (Rusinkiewicz and Levoy 2001). The implementation described here includes a Sobolev smoothing constraint for sparse and scattered data and has been previously illustrated for fitting anatomically based bicubic-Hermite surface meshes (Young, Hunter and Smaill 1989, Bradley *et al.* 1997). Here, its implementation for fitting faces of three-dimensional volume meshes is given. The

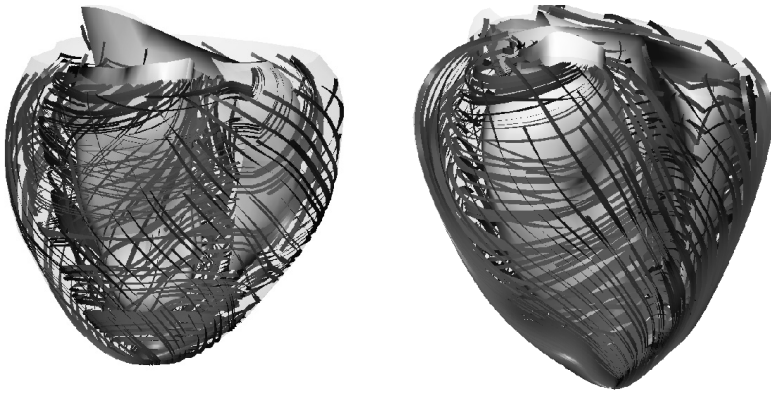

(a) (b)

Figure 2.5. Anatomically accurate canine (a) and porcine (b) finite element models. Two layers of streamlines (one on the outer epicardial surface and one midway through the wall) are used to visualize the epicardial and midwall fibre directions which vary continuously through the wall.

nodal positions of this mesh are optimized to achieve the minimum distance between data points and the closest face of the mesh. This is done by minimizing an objective function based on an L_2 distance norm, calculated from projections of the data points on to the mesh faces.

The data for this fitting process are generated from a number of different sources, dependent on organ type and species. Data for human models are typically created by digitizing slices from the Visible Human (VH) database, which has become a common standard for researchers and provides a way of comparing and sharing geometries (Ackerman 1998). Non-invasive imaging techniques such as Magnetic Resonance Imaging (Young, Fayad and Axel 1996) and Computed Tomography (Kantor *et al.* 1999) provide additional and expanding sources of data. Animal models of organs such as the heart have been measured directly (Nielsen *et al.* 1991, Vetter and McCulloch 2000) and have also been measured from casts taken of the heart (Kassab, Rider, Tang and Fung 1993).

An initial mesh topology is extracted from the cloud of data points by selecting data points on the outside of the data cloud. These serve as nodes for the mesh which are then used to generate elements in a systematic manner. The nodes are chosen to construct a regular mesh with the minimal number of elements.

Data projection

The digitization process generates a Cartesian data set with geometric positions $\boldsymbol{z}_d, d = 1, \ldots, N$. For each data point we can find the position on a given two-dimensional mesh face which has the smallest distance to the data point. This position is the orthogonal projection of the data point on to the mesh and has geometric position $\boldsymbol{u} = \boldsymbol{x}$. The point $\boldsymbol{x}$ is also given by the local element coordinate $\boldsymbol{\xi}_d$ as is shown in Figure 2.6. A least-squares distance function, D, between a data point and its projection may be expressed by

$$D(\xi_1, \xi_2) = \|\boldsymbol{x}(\xi_1, \xi_2) - \boldsymbol{z}_d\|^2, \tag{2.7}$$

where $\boldsymbol{z}_d$ are the spatial coordinates of the data point and $\boldsymbol{x}(\xi_1, \xi_2)$ is interpolated using a bicubic-Hermite basis function which is a reduced form of equation (2.3):

$$\begin{aligned}\boldsymbol{x}(\xi_1, \xi_2) = \sum_{j=1}^{2}\sum_{i=1}^{2}\Bigg[& H_i^0(\xi_1)H_j^0(\xi_2)\boldsymbol{x}_n + H_i^1(\xi_1)H_j^0(\xi_2)\left(\frac{\partial \boldsymbol{x}}{\partial \xi_1}\right)_n \\ & + H_i^0(\xi_1)H_j^1(\xi_2)\left(\frac{\partial \boldsymbol{x}}{\partial \xi_2}\right)_n + H_i^1(\xi_1)H_j^1(\xi_2)\left(\frac{\partial^2 \boldsymbol{x}}{\partial \xi_1 \partial \xi_2}\right)_n\Bigg]\end{aligned} \tag{2.8}$$

with the derivatives with respect to ξ converted using

$$\left(\frac{\partial \boldsymbol{x}}{\partial \xi_\alpha}\right) = \left(\frac{\partial \boldsymbol{x}}{\partial s_\alpha}\right)\left(\frac{\partial s_\alpha}{\partial \xi_\alpha}\right),$$

and

$$\left(\frac{\partial^2 \boldsymbol{x}}{\partial \xi_\alpha \partial \xi_\beta}\right) = \left(\frac{\partial^2 \boldsymbol{x}}{\partial s_\alpha \partial s_\beta}\right)\left(\frac{\partial s_\alpha}{\partial \xi_\alpha}\right)\left(\frac{\partial s_\beta}{\partial \xi_\beta}\right),$$

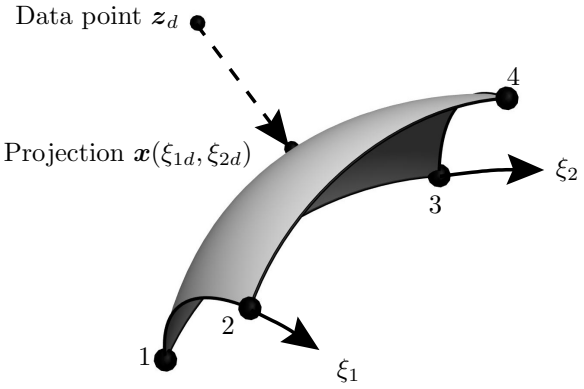

Figure 2.6. Projection of data point $\boldsymbol{z}_d$ on to an element face and the resulting closest point $\boldsymbol{x}(\xi_{1d}, \xi_{2d})$.

for cross-derivatives ($\alpha, \beta = 1, 2$ where no summation is implied). Note $\boldsymbol{x}(\xi_1, \xi_2)$ here refers to the continuum field evaluated at material points ξ_1, ξ_2, while $\boldsymbol{x}_n$ refers to the vector of nodal parameters used in the interpolation. Thus the local coordinates of the projection point (ξ_{1d}, ξ_{2d}), and hence its global coordinates, can be determined by solving the following nonlinear simultaneous equations using the Newton–Raphson procedure:

$$\frac{\partial D}{\partial \xi_1} = 0, \qquad \frac{\partial D}{\partial \xi_2} = 0. \tag{2.9}$$

Objective function minimization

For a given projection of the data points on to the mesh (*i.e.*, $\boldsymbol{\xi}_d$ is held constant), the objective function to be minimized is the sum-of-squares of the individual errors

$$F(\bar{\boldsymbol{x}}) = \sum_{d=1}^{N} w_d \|\boldsymbol{x}(\xi_{1d}, \xi_{2d}) - \boldsymbol{z}_d\|^2, \tag{2.10}$$

where w_d is a weight for each data point and $\bar{\boldsymbol{x}}$ is a vector of mesh parameters. Weights w_d are set to unity unless there is a clear difference in quality of the data (*e.g.*, when combining data sets acquired using different methods).

The fitting problem is to find the set of mesh parameters that minimizes this objective function. For simplicity the formulation of the linear system is illustrated below for a one-dimensional element, and the two- and three-dimensional formulations can be inferred.

Substituting equation (2.8) into equation (2.10) and differentiating, we obtain

$$\frac{\partial F}{\partial \bar{x}_m} = 2 \sum_{d=1}^{N} w_d \left(\sum_{r=1}^{4} \psi_r(\xi_d) \bar{x}_r - z_d \right) \psi_m(\xi_d), \tag{2.11}$$

where the functions ψ are calculated from the products of the Hermite basis functions formed in equation (2.8). A minimum of the objective function can thus be found by setting the partial derivatives in equation (2.11) to zero. This will result in a linear system only if the scale factors are kept constant during the fit; that is, the vector $\bar{\boldsymbol{x}}$ will contain the nodal positions and the nodal arclength derivatives. With this restriction we can obtain a linear system of equations of the form $A_{rm} \bar{x}_r = b_m$ where

$$A_{rm} = \sum_{d=1}^{N} w_d \sum_{r=1}^{4} \psi_r(\xi_d) \psi_m(\xi_d), \tag{2.12}$$

$$b_m = \sum_{d=1}^{N} w_d \psi_m(\xi_d) z_d, \tag{2.13}$$

and N is the total number of data points.

A linear system of equations governing the entire mesh can then be found by assembling a global stiffness matrix from all the element matrices, and solved to yield new nodal positions, derivatives and scale factors. The updated scale factors alter the shape of the mesh, since the scale factors are involved explicitly in the interpolation functions as described in equation (2.8). The steps described above are therefore repeated until convergence is achieved.

Sobolev smoothing

To deal with an insufficient number of data points, fitting noisy data or fitting data that has an uneven spread (see Figure 2.7), a smoothness constraint (Young *et al.* 1989) can be introduced by adding a second term to the objective function equation (2.10). This is known as Sobolev smoothing with a penalty function, in two dimensions, of the form

$$F_s(\boldsymbol{x}) = \int_0^1\int_0^1 \left\{ \alpha_1 \left\| \frac{\partial \boldsymbol{x}}{\partial \xi_1} \right\|^2 + \alpha_2 \left\| \frac{\partial \boldsymbol{x}}{\partial \xi_2} \right\|^2 + \alpha_3 \left\| \frac{\partial^2 \boldsymbol{x}}{\partial \xi_1^2} \right\|^2 + \alpha_4 \left\| \frac{\partial^2 \boldsymbol{x}}{\partial \xi_2^2} \right\|^2 + \alpha_5 \left\| \frac{\partial^2 \boldsymbol{x}}{\partial \xi_1 \partial \xi_2} \right\|^2 \right\} \mathrm{d}\xi_1\, \mathrm{d}\xi_2, \tag{2.14}$$

where α_i $(i = 1, \ldots, 5)$ are the Sobolev weights (penalty parameters). Each term has a distinct effect on the final shape of the fitted object. The first two terms (α_1, α_2) control the arclength, while the third and fourth terms (α_3, α_4) control the arc curvature in the ξ_1 and ξ_2 directions, respectively. The last term (α_5) represents the face area. For instance, if the weight

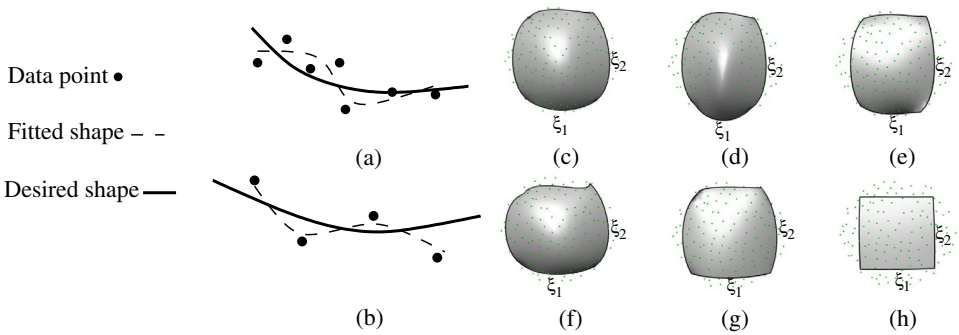

Figure 2.7. Unbiased fitting due to (a) scattered, and (b) sparse data. Effects of Sobolev weights in a 2D surface fit with (c) no smoothing (d) ξ_1 weighting on α_1 and (e) weighting on α_1 and α_3. (f), (g) show similar behaviour for the ξ_2 direction and (h) shows weighting on all faces including the area term α_5.

associated with the cross-derivative term is set to a high value, one might expect to end up with a mesh with a smaller face area.

The effect of these parameters is illustrated for a simple two-dimensional surface in Figure 2.7(c)–(h). Figure 2.7(c) shows the effect with no smoothing. Increasing α_1 reduces the arclength in the ξ_1 direction (Figure 2.7(d)) and including α_3 reduces the ξ_1 curvature which is seen as a flattening in this direction (Figure 2.7(e)). Similar behaviour is observed for the ξ_2 direction (Figure 2.7(f), (g)). Placing weights on all coefficients including the area term (α_5) causes a smooth reduction in the face area (Figure 2.7(h)).

3. Continuum modelling

The development of whole organ models using the above anatomically based finite element descriptions of geometry and tissue microstructure requires two further steps. Firstly, the cellular-based processes which produce a change in the state of the organ system, independent of the variations in boundary conditions, must be characterized. These cellular-based models are introduced in Section 4. Secondly, governing equations must be proposed which relate material properties to continuum tissue behaviour. Specifically, the numerical frameworks for applying equations determining deformation and activation are outlined below in Sections 3.1 and 3.2.

3.1. Finite deformation mechanics

Understanding and predicting the deformation of tissue under varying distributions of applied stresses and strains is fundamental to understanding its function. To deal with the nonlinear constitutive mechanical behaviour requires a framework based on finite deformation mechanics.

Kinematics

We begin by introducing the kinematic relations required to track material based properties through large deformations. Let $\boldsymbol{x} = (x_1, x_2, x_3)$ give the present position in rectangular Cartesian coordinates of a material particle that occupied the position $\mathbf{X} = (X_1, X_2, X_3)$ in the reference state.

In standard finite deformation theory (x_1, x_2, x_3) are considered as material coordinates and a *deformation gradient tensor* $\mathbf{F}$ is defined, which carries the undeformed line segment, $\mathrm{d}\mathbf{X}$, to the corresponding deformed line segment $\mathrm{d}\mathbf{x} = \mathbf{F}\,\mathrm{d}\mathbf{X}$, or in component form:

$$\mathrm{d}x^i = F^i_M\,\mathrm{d}X^M, \tag{3.1}$$

where

$$F^i_M = \frac{\partial x_i}{\partial X_M}. \tag{3.2}$$

Polar decomposition, $\mathbf{F} = \mathbf{RU}$, splits $\mathbf{F}$ into the product of an orthogonal rotation tensor, $\mathbf{R}$, and a symmetric positive definite stretch tensor, $\mathbf{U}$, which contains a complete description of the material strain, independent of any rigid body motion (Atkin and Fox 1980).

For inhomogeneous, anisotropic materials the orientation of the material axes may vary with location, for example fibre direction changes spatially throughout the myocardium. Thus it is no longer practical to identify the material axes in the undeformed body with the reference coordinates (X_1, X_2, X_3). Instead, a new material coordinate system (ν_1, ν_2, ν_3) is introduced which is aligned with the microstructural features of the material, as described above in Section 2.1. For myocardium, a natural set of material axes are formed by identifying ν_1 with the muscle fibre direction, ν_2 with the sheet direction and ν_3 with the sheet-normal direction.

It is useful to choose the base vectors for the ν_α-coordinate system to be orthogonal in the reference state. This is convenient in myocardium, for example, where the ν_α-coordinates are chosen to line up with the fibre, sheet and sheet-normal directions, which are defined to be orthogonal in the undeformed state. However, the ensuing deformation means that they are not, in general, orthogonal in the deformed configuration.

$\mathbf{A}_\alpha^{(\nu)}$, $\mathbf{A}^\alpha_{(\nu)}$ and $\mathbf{a}_\alpha^{(\nu)}$, $\mathbf{a}^\alpha_{(\nu)}$ denote the covariant and contravariant base vectors in the undeformed and deformed configurations, respectively. The corresponding metric tensors are denoted by $A^{(\nu)}_{\alpha\beta}$, $A^{\alpha\beta}_{(\nu)}$ and $a^{(\nu)}_{\alpha\beta}$, $a^{\alpha\beta}_{(\nu)}$. The undeformed covariant base vectors, $\mathbf{A}_\alpha^{(\nu)}$, are defined to be unit vectors by choosing the ν_α-coordinates to be a measure of physical arclength in the undeformed state. The base vectors and metric tensors for the ν_α-coordinate system are

$$\begin{aligned} \mathbf{A}_\alpha^{(\nu)} &= \frac{\partial X_k}{\partial \nu_\alpha}\mathbf{g}_k^{(x)}, & \mathbf{a}_\alpha^{(\nu)} &= \frac{\partial x_k}{\partial \nu_\alpha}\mathbf{g}_k^{(x)}, \\ A^{(\nu)}_{\alpha\beta} &= \mathbf{A}_\alpha^{(\nu)} \cdot \mathbf{A}_\beta^{(\nu)}, & a^{(\nu)}_{\alpha\beta} &= \mathbf{a}_\alpha^{(\nu)} \cdot \mathbf{a}_\beta^{(\nu)}, \end{aligned} \tag{3.3}$$

where $\mathbf{g}_k^{(x)}$ are the base vectors of the rectangular Cartesian reference axes. The Green strain tensor, defining the kinematics of large deformation for an inhomogeneous anisotropic material, is then

$$E_{\alpha\beta} = \frac{1}{2}\Big(a^{(\nu)}_{\alpha\beta} - A^{(\nu)}_{\alpha\beta}\Big). \tag{3.4}$$

Stress equilibrium and the principle of virtual work

The governing equations for elastostatics can be derived from a physically appealing argument. For equilibrium, the work done by the external surface forces in moving through a virtual displacement is equal to the work done

by the stress vector in moving through a compatible set of virtual displacements. Using this principle (known as the principle of virtual work) the stress equilibrium can be expressed via the following equation (Nash and Hunter 2000):

$$\int_{V_0} T^{\alpha\beta} F^j_\beta \delta v_j \big|_\alpha \, \mathrm{d}V_0 = \int_{V_0} \rho_0 \left(b^j - f^j\right) \delta v_j \, \mathrm{d}V_0 + \int_{S_2} p_{(\mathrm{appl})} \frac{g^{3M}_{(\xi)}}{\sqrt{g^{33}_{(\xi)}}} \frac{\partial x_j}{\partial \xi_M} \, \delta v_j \, \mathrm{d}S \tag{3.5}$$

where $T^{\alpha\beta}$ are second Piola–Kirchhoff stresses expressed relative to the fibre-sheet material coordinates; $\big|_\alpha$ is a covariant derivative; $\delta\mathbf{v} = \delta v_j \mathbf{i}_j$ are virtual displacements expressed relative to the reference coordinate system (Malvern 1969); b^j and f^j are the components of the body force and acceleration vectors, respectively; $p_{(\mathrm{appl})}$ is the pressure applied to the surface S_2 with normal direction ξ_3; ρ_0 is the tissue density; and $g^{MN}_{(\xi)}$ are contravariant metric tensors for the ξ_i-coordinate system. Covariant base vectors and metric tensors for the ξ_M-coordinate system are defined for the undeformed and deformed states as follows:

$$\begin{aligned} \mathbf{G}^{(\xi)}_M &= \frac{\partial X_k}{\partial \xi_M} \mathbf{g}^{(x)}_k, & \mathbf{g}^{(\xi)}_M &= \frac{\partial x_k}{\partial \xi_M} \mathbf{g}^{(x)}_k, \\ G^{(\xi)}_{MN} &= \mathbf{G}^{(\xi)}_M \cdot \mathbf{G}^{(\xi)}_N = \frac{\partial X_k}{\partial \xi_M} \frac{\partial X_k}{\partial \xi_N}, & g^{(\xi)}_{MN} &= \mathbf{g}^{(\xi)}_M \cdot \mathbf{g}^{(\xi)}_N = \frac{\partial x_k}{\partial \xi_M} \frac{\partial x_k}{\partial \xi_N}. \end{aligned} \tag{3.6}$$

Equation (3.5) is the starting point for the analysis of a body undergoing large elastic deformations. For further detail see Costa *et al.* (1996*a*, 1996*b*).

Finite element solution techniques

Using the interpolation functions ψ_n from Section 2.1 we can define virtual displacement fields δv_j as

$$\delta v_j = \psi_n \left(\xi_1, \xi_2, \xi_3\right) \delta v^n_j, \tag{3.7}$$

where δv^n_j are arbitrary virtual nodal displacements. Substituting equation (3.7) into the equilibrium equations (equation (3.5)) and setting the coefficient of each component δv^n_j to zero, gives

$$\int_{V_0} T^{\alpha\beta} F^j_\beta \psi_n \big|_\alpha \, \mathrm{d}V_0 = \int_{V_0} \rho_0 \left(b^j - f^j\right) \psi_n \, \mathrm{d}V_0 + \int_{S_2} p_{(\mathrm{appl})} \frac{g^{3M}_{(\xi)}}{\sqrt{g^{33}_{(\xi)}}} \frac{\partial x_j}{\partial \xi_M} \, \psi_n \, \mathrm{d}S. \tag{3.8}$$

To evaluate the integrals in equation (3.8), they must first be transformed from the reference coordinate space to the ξ_M-coordinate space using the

appropriate Jacobian. The transformed integrals are written in (3.9):

$$\iiint_{V_0} T^{\alpha\beta} F^j_\beta \psi_n \big|_\alpha \sqrt{G^{(\xi)}}\, \mathrm{d}\xi_3\, \mathrm{d}\xi_2\, \mathrm{d}\xi_1 \tag{3.9}$$
$$= \iiint_{V_0} \rho_0 \left(b^j - f^j\right) \psi_n \sqrt{G^{(\xi)}}\, \mathrm{d}\xi_3\, \mathrm{d}\xi_2\, \mathrm{d}\xi_1 + \iint_{S_2} p_{(\mathrm{appl})}\; g^{3M}_{(\xi)}\; \frac{\partial \theta_j}{\partial \xi_M}\; \psi_n \sqrt{g^{(\xi)}}\, \mathrm{d}\xi_2\, \mathrm{d}\xi_1,$$

where $\sqrt{G^{(\xi)}} = \sqrt{\det\{G^{(\xi)}_{ij}\}}$ and $\sqrt{g^{(\xi)}} = \sqrt{\det\{g^{(\xi)}_{ij}\}}$ are the Jacobians of the three-dimensional coordinate transformation with respect to the undeformed and deformed configurations, respectively. Note that the surface integral is transformed by substituting $J_{2D}\, \mathrm{d}\xi_2\, \mathrm{d}\xi_1$ for $\mathrm{d}S$, where the two-dimensional Jacobian with respect to deformed coordinates is given by $J_{2D} = \sqrt{g^{(\xi)} g^{33}_{(\xi)}}$ (Oden 1972).

The three-dimensional integrals in equation (3.9) are evaluated over the undeformed volume and the two-dimensional integral is computed over the portion of the deformed surface (denoted S_2) for which external pressure loads are applied. These integrals are replaced by a sum of integrals over the collection of element domains which constitute the finite element model. Element integrals are evaluated numerically using Gaussian quadrature. Components of the second Piola–Kirchhoff stress tensor, $T^{\alpha\beta}$, are evaluated at each Gauss point using (Malvern 1969)

$$T^{\alpha\beta} = \frac{1}{2}\left(\frac{\partial W}{\partial E_{\alpha\beta}} + \frac{\partial W}{\partial E_{\beta\alpha}}\right) - p a^{\alpha\beta}_{(\nu)}, \tag{3.10}$$

where p is hydrostatic pressure and the derivatives of the strain energy function W with respect to the components of $\boldsymbol{E}$ are determined using a constitutive relation.

The strain energy functions of cardiac tissue have been characterized and applied by a number of authors (Guccione, McCulloch and Waldman 1991, Emery, Omens and McCulloch 1997, Usyk, Le Grice and McCulloch 2002) using a generic exponential relation of the form

$$W = \frac{1}{2}\boldsymbol{C}(\mathrm{e}^Q - 1), \tag{3.11}$$

where $\boldsymbol{C}$ is the right Cauchy–Green strain tensor and Q is a function in which the strain components of $\boldsymbol{E}$ are referred to the local structure-based coordinates. Guccione *et al.* (1991) defined the form of Q such that myocardium was assumed to be transversely isotropic and incompressible. More recently Usyk, Mazhari and McCulloch (2000) have developed and applied (Usyk *et al.* 2002) a fully orthotropic model in the form of equation (3.11) within a three-dimensional model of cardiac mechanics. Difficulties lie in

assigning unique parameter values in the complex forms of Q required to fully represent the orthotropic behaviour of myocardium via equation (3.11).

The passive myocardial characteristics have also been encapsulated via an alternative *pole-zero* strain energy function for the myocardium (Hunter, Smaill and Hunter 1995) given by

$$\begin{aligned} W &= k_{11}\frac{E_{11}^2}{|a_{11}-E_{11}|^{b_{11}}} + k_{22}\frac{E_{22}^2}{|a_{22}-E_{22}|^{b_{22}}} + k_{33}\frac{E_{33}^2}{|a_{33}-E_{33}|^{b_{33}}} \\ &+ k_{12}\frac{E_{12}^2}{|a_{12}-E_{12}|^{b_{12}}} + k_{13}\frac{E_{13}^2}{|a_{13}-E_{13}|^{b_{13}}} + k_{23}\frac{E_{23}^2}{|a_{23}-E_{23}|^{b_{23}}} \end{aligned} \quad (3.12)$$

where the constitutive parameters (as, bs and ks) are fitted from biaxial testing of tissue slices cut parallel with the fibre axis at several transmural sites throughout the myocardium (Novak, Yin and Humphrey 1994). Within equation (3.12) $a_{\alpha\beta}$ denote limiting strain or poles, $b_{\alpha\beta}$ relate the curvature of the uni-axial stress–strain relationships and $k_{\alpha\beta}$ weight the contribution of the corresponding mode of deformation to the total strain energy of the material.

For incompressible materials, an additional scalar hydrostatic pressure field is introduced into the constitutive equations. The extra constraint necessary to determine the parameters of the hydrostatic pressure field arise from the requirement that the third strain invariant (I_3) equals one for incompressible materials.

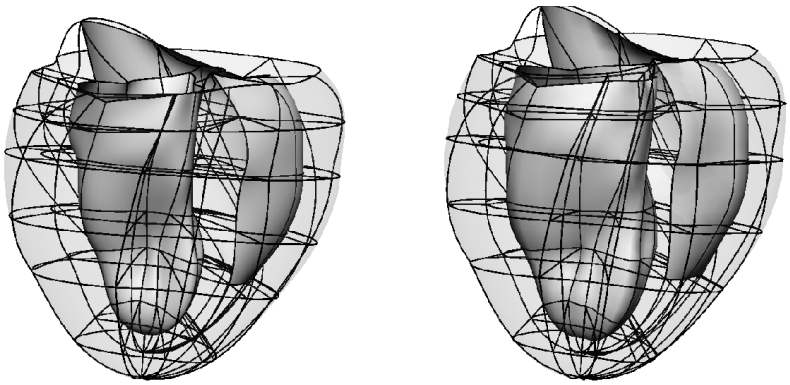

(a) (b)

Figure 3.1. (a) Canine finite element model in its reference state. (b) Geometry calculated from application of cavity pressures to simulate inflation.

For a Galerkin formulation, the form of the incompressibility constraints is given in equation (3.13):

$$\iiint_{V_e} (\sqrt{I_3} - 1)\psi^p \sqrt{G^{(\xi)}}\, \mathrm{d}\xi_3\, \mathrm{d}\xi_2\, \mathrm{d}\xi_1 = 0, \tag{3.13}$$

where V_e denotes the domain of the element and ψ^p are the basis functions used to approximate the three-dimensional hydrostatic pressure field. Note that the undeformed three-dimensional Jacobian, $\sqrt{G^{(\xi)}}$, is introduced since the integrals are evaluated with respect to the undeformed configuration.

The methods outlined above can be applied to calculate the deformations associated with inflation of the finite element mesh of the canine ventricular model shown in Figure 3.1. The reference geometry is shown in Figure 3.1(a), and the deformed geometry produced by the application of left and right cavity ventricular pressures of 0.2 kPa and 1 kPa, respectively, is shown in Figure 3.1(b).

Numerical and computational issues

There are a number of numerical and computational challenges which must be overcome for the effective and efficient application of the finite element method to the finite deformation mechanics equations described above. The first of these is in the implementation of numerical techniques to find the roots of the system of nonlinear equations obtained by evaluating the integrals in equations (3.9) and (3.13) for each element in the mesh. The Newton–Raphson method can be used for this root-finding process. The calculation of the Newton step vector at each iteration requires the solution of a sparse set of linear equations, for which the *SuperLU* method (Demmel *et al.* 1999*a*, Demmel, Gilbert and Li 1999*b*) has been found to perform well.

Oden (1972) suggests that the interpolation scheme chosen to describe the deformed geometric coordinates (ψ_n in equation (3.9)) should be of higher order than those chosen to approximate the hydrostatic pressure field (ψ^p in equation (3.13)). The strain energy contribution to stress components is related to the first derivatives of the geometric displacement fields, whereas the hydrostatic pressure directly contributes to the stress components. For consistency, and to avoid numerical ill-conditioning when calculating components of the stress tensor, the two contributions should vary in a similar manner.

The computational issues associated with modelling finite deformation mechanics centre around the exploitation of parallel architectures. In particular, the determination of groups of element stiffness matrices can be allocated across multiple processors while incurring only a small computational overhead. Furthermore, the *SuperLU* algorithm provides close-to-linear scalability for the Newton step calculations. The scalability of two such major components of the method means that, with increased

processor count, close-to-linear speed-up is exhibited for the whole algorithm. The ease of implementation and code maintenance for shared memory architectures is well suited to finite deformation mechanics simulations, and indeed this has been the preferred platform. However, recent improvements in availability and the ongoing optimization of specific algorithms (Li and Demmel 2003) mean that distributed memory systems now provide an increasingly attractive alternative computational platform.

3.2. Myocardial activation

Cardiac tissue consists of discrete cells but we can model the electrical behaviour of the tissue using a continuum approach that averages the electrical properties over a length scale greater than that of single cells. In the continuum approach we assume that cardiac tissue has three orthogonal conductivity directions following the microstructural organization of the tissue. The fastest conductivity is along the fibre axis; there is slower conductivity in the plane of the sheet, and finally the slowest propagation is along the sheet-normal axis.

The continuum approach uses the bidomain model of multicellular volume conductors, which has been used extensively in models of the spread of electrical activity in excitable tissues (Fischer *et al.* 2000, Henriquez 1993, Muzikant and Henriquez 1998, Plonsey and Barr 1984, Roth and Wikswo 1986, Roth 1997, Skouibine, Trayanova and Moore 2000, Trayanova 1994). The bidomain model of cardiac tissue consists of two interpenetrating domains representing cells and the space surrounding them. The intracellular domain represents the region inside the cells and is given the subscript i, and the extracellular domain represents the space between cells and is given the subscript e. The key to the model is that these two domains are assumed to exist at all points in the physical solution domain. Detailed derivation of the bidomain model can be found elsewhere (Schmitt 1969, Tung 1978, Krassowska and Neu 1994). Here we state the equations and show how they are transformed into finite element coordinates in order to study electrical propagation on a deforming finite element mesh.

Let ϕ_i and ϕ_e be the electric potentials in the intracellular and extracellular domains, respectively, and $V_m = \phi_i - \phi_e$ is the transmembrane potential. Associated with these domains are the macroscopic tensor quantities σ_i and σ_e, representing the local volume averaged conductivities in the intra- and extracellular spaces, respectively. Tensors σ_i and σ_e are each separately anisotropic and are assumed to be diagonal in the material coordinates based on the fibrous structure of muscle tissue.

The bidomain model consists of two equations. The first describes the conservation of current,

$$\nabla \cdot ((\sigma_i + \sigma_e)\nabla\phi_e) = -\nabla \cdot (\sigma_i \nabla V_m) + I_{s1}, \tag{3.14}$$

that given a transmembrane potential distribution is used to solve for the extracellular potential. The second equation describes the current flow across the cellular membrane composed of ionic and capacitive currents (the cell membrane acts as a parallel capacitance), that is,

$$\nabla \cdot (\sigma_i \nabla V_m) + \nabla \cdot (\sigma_i \nabla \phi_e) = A_m \left(C_m \frac{\partial V_m}{\partial t} + I_{\text{ion}} \right) - I_{s2}, \tag{3.15}$$

and is used to calculate the transmembrane potential distribution. A_m is the surface to volume ratio of the cell membrane, C_m is the membrane capacitance per unit area, and I_{ion} is a nonlinear function representing the sum of all the transmembrane ionic currents. Externally applied volume stimulus currents can be imposed in both the extracellular (I_{s1}) and intracellular (I_{s2}) domains.

It is assumed that there is no current flow between the intracellular domain and the external region so the boundary condition applied to V_m on the solution domain boundary is

$$(\sigma_i \nabla V_m) \cdot \boldsymbol{n} = -(\sigma_i \nabla \phi_e) \cdot \boldsymbol{n}, \tag{3.16}$$

where $\boldsymbol{n}$ is a unit vector outwardly normal to the domain boundary. For the extracellular domain the current must balance between the extracellular domain and the surrounding external regions, that is,

$$(\sigma_e \nabla \phi_e) \cdot \boldsymbol{n} = -(\sigma_o \nabla \phi_o) \cdot \boldsymbol{n}, \tag{3.17}$$

where σ_o signifies the conductivity of the surrounding region. The negative sign accounts for the direction of current flow as both sides of the equations use outward normal vectors. The boundary extracellular potential must also match the potential of the boundary of the external regions,

$$\phi_e = \phi_o. \tag{3.18}$$

In the absence of an external region any combination of current and potential boundary conditions can be used to specify the required physical problem, with the restriction that at least one extracellular boundary point has a potential boundary condition to provide a reference potential (and hence a unique solution to the bidomain equations).

The monodomain model of activation

In an effort to further reduce the computational cost of the activation modelling, the extracellular domain is sometimes assumed to be highly conducting or, alternatively, both domains are assumed equally anisotropic. With either of these assumptions the transmembrane potential is equal to the intracellular potential, and the bidomain equations simplify to

$$\nabla \cdot (\sigma \nabla V_m) = A_m \left(C_m \frac{\partial V_m}{\partial t} + I_{\text{ion}} \right) - I_s, \tag{3.19}$$

as the gradient of the extracellular potential field is effectively zero in either of these approximations. This monodomain model is suitable for situations such as computations on an isolated heart. When the extracellular electrical state is important the full bidomain model needs to be used, for example electrical current propagating from the heart to the torso in body surface potential forward simulations or the application of defibrillation-type extracellular stimuli.

For the monodomain model, there is no connection between the intracellular domain and any surrounding media. Therefore, no current can flow out of the solution domain, giving rise to the boundary condition

$$(\sigma \nabla V_m) \cdot \boldsymbol{n} = 0. \tag{3.20}$$

Finite element-derived finite difference method

In order to solve the bidomain or monodomain models on realistic ventricular geometry domains, the equations need to be solved numerically, dividing the solution domain into smaller subdomains over which the equations can be integrated. The method reviewed here for the numerical integration of the bidomain or monodomain models is a collocation method known as the finite element-derived finite difference method (Buist, Sands, Hunter and Pullan 2003). In this method, finite elements (FEs) are used to describe the tissue geometry and fibrous microstructure, and the activation equations are solved on a high-resolution nonuniform finite difference (FD) grid which is defined from and embedded in the material space of the FEs. This allows for the much smaller space constant required for the resolution of local behaviour and steep spatial gradients of the activation model while having the solution mesh defined by the geometry of the problem, including any geometric deformation applied to the host FE mesh as the points remain invariant in material space.

A significant advantage of this method is that the FD collocation points are embedded in the FE geometric mesh, so when the geometric mesh deforms (*i.e.*, due to contraction of muscle) the FD points move with the deformation. This is an essential feature when modelling coupled electromechanics, as seen in the following section (Section 3.3). Figure 3.2 illustrates the definition of such FD meshes and their mapping to the local quadratic solution space (Buist *et al.* 2003).

To solve the bidomain equations (3.14) and (3.15) or monodomain equation (3.19) we need to express the diffusion terms $\nabla \cdot (\sigma \nabla \phi)$ in the curvilinear material coordinates (ξ_1, ξ_2, ξ_3). The expansion of this term using domain metrics and standard tensor notation, with a comma denoting partial differentiation, gives

$$\nabla \cdot (\sigma \nabla \phi) = \left(\sigma^k_{\alpha,\beta} \phi_{,k} + \sigma^k_\alpha \phi_{,k\beta} - \sigma^k_l \phi_{,k} \Gamma^l_{\alpha\beta}\right) a^{\beta\alpha}_{(\nu)}, \tag{3.21}$$

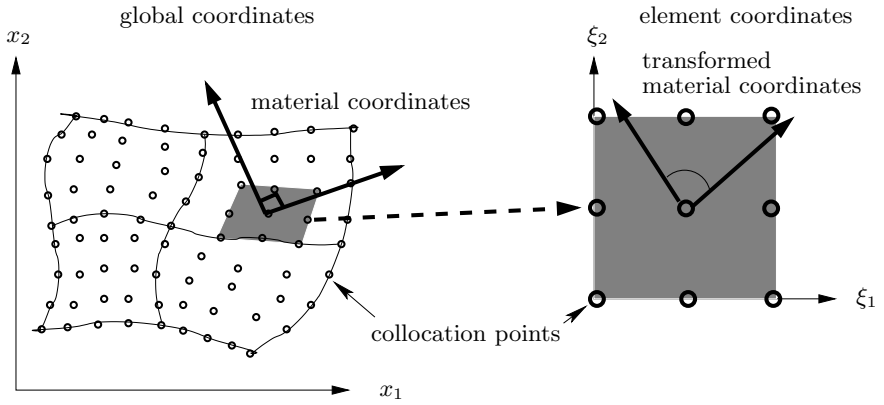

Figure 3.2. An illustration of the collocation points defined on a two-dimensional finite element mesh. Each interior point together with its 8 surrounding points (in 2D (x_1, x_2)-space) is mapped on to a unit square in (ξ_1, ξ_2)-space. Note that the material coordinates which are orthogonal in (x_1, x_2)-space become non-orthogonal in (ξ_1, ξ_2)-space.

where $a^{\beta\alpha}_{(\nu)}$ are the components of the contravariant metric tensor in the deformed configuration which is defined in terms of the contravariant base vectors

$$a^{\beta\alpha}_{(\nu)} = \boldsymbol{a}^{\beta}_{(\nu)} \cdot \boldsymbol{a}^{\alpha}_{(\nu)}. \tag{3.22}$$

See equation (3.3) for more detail. The Christoffel symbol $(\Gamma^{l}_{\alpha\beta})$ is used to represent the base vector derivatives and is defined as

$$\Gamma^{l}_{\alpha\beta} = \boldsymbol{a}^{(\xi)}_{\alpha,\beta} \cdot \boldsymbol{a}^{l}_{(\xi)}. \tag{3.23}$$

Tissue microstructure

The tissue microstructure is included in the activation model through the extra- and intracellular conductivity tensors (σ_e, σ_i). Using the material coordinate system (ν_1, ν_2, ν_3) defined previously, the original conductivity tensor $(\sigma^{*a}_{\ b})$ is a diagonal tensor given by

$$\sigma^{*a}_{\ b} = \begin{pmatrix} \sigma_f & 0 & 0 \\ 0 & \sigma_s & 0 \\ 0 & 0 & \sigma_c \end{pmatrix}, \tag{3.24}$$

where σ_f is the fibre direction conductivity, σ_s the sheet, and σ_c the cross-sheet conductivity. For direct inclusion into equation (3.21) $\sigma^{*a}_{\ b}$ must be

transformed into ξ_j coordinates (Figure 3.2). This is accomplished with the transformation

$$\sigma_j^k = \frac{\partial \xi_k}{\partial \nu_a} \frac{\partial \nu^b}{\partial \xi_j} \sigma^{*a}{}_b. \tag{3.25}$$

The resulting effective conductivity tensor σ_j^k is, in general, no longer diagonal.

Numerical solution

As shown in Figure 3.2, each interior FD point is mapped into a local quadratic template element consisting of the surrounding FD points in order to approximate the first- and second-order partial derivatives of potential and the first-order partial derivative of the conductivity tensors. The quadratic basis is chosen simply to ensure second-order accuracy in the spatial derivatives used for the reaction–diffusion equations. The three quadratic Lagrange basis functions in one dimension are

$$\begin{aligned} \psi_1(\xi) &= 2\left(\xi - \frac{1}{2}\right)(\xi - 1), \\ \psi_2(\xi) &= -4\xi\,(\xi - 1), \\ \psi_3(\xi) &= 2\xi\left(\xi - \frac{1}{2}\right). \end{aligned} \tag{3.26}$$

Basis functions for higher dimensions are created through the tensor product of these one-dimensional basis functions. Quadratic basis functions of the appropriate dimension are then used to interpolate over the local quadratic element, in a manner similar to that already discussed in Section 2.1.

From the central node in the local quadratic element, the indices i, j, and k are used to denote steps in the ξ_1, ξ_2, and ξ_3 directions, respectively, where a single step can be made in each of the positive and negative directions. With this template, each of the partial derivatives in equation (3.21) can be approximated by quadratic basis function derivatives where the central node has a location of $\xi = \frac{1}{2}$ in each of the local element directions. The three first-order derivatives of potential are

$$\begin{aligned} \frac{\partial \phi}{\partial \xi_1} &= \phi_{(i+1)(j)(k)} - \phi_{(i-1)(j)(k)}, \\ \frac{\partial \phi}{\partial \xi_2} &= \phi_{(i)(j+1)(k)} - \phi_{(i)(j-1)(k)}, \\ \frac{\partial \phi}{\partial \xi_3} &= \phi_{(i)(j)(k+1)} - \phi_{(i)(j)(k-1)}. \end{aligned} \tag{3.27}$$

The first-order derivatives of the conductivity tensor components are found

in a similar way. The second-order derivatives are defined as

$$\begin{aligned}
\frac{\partial^2\phi}{\partial\xi_1^2} &= 4\big(\phi_{(i+1)(j)(k)} - 2\phi_{(i)(j)(k)} + \phi_{(i-1)(j)(k)}\big),\\
\frac{\partial^2\phi}{\partial\xi_2^2} &= 4\big(\phi_{(i)(j+1)(k)} - 2\phi_{(i)(j)(k)} + \phi_{(i)(j-1)(k)}\big),\\
\frac{\partial^2\phi}{\partial\xi_3^2} &= 4\big(\phi_{(i)(j)(k+1)} - 2\phi_{(i)(j)(k)} + \phi_{(i)(j)(k-1)}\big),
\end{aligned} \tag{3.28}$$

with three cross-derivative terms:

$$\begin{aligned}
\frac{\partial^2\phi}{\partial\xi_1\partial\xi_2} &= \phi_{(i+1)(j+1)(k)} - \phi_{(i+1)(j-1)(k)} - \phi_{(i-1)(j+1)(k)} + \phi_{(i-1)(j-1)(k)},\\
\frac{\partial^2\phi}{\partial\xi_1\partial\xi_3} &= \phi_{(i+1)(j)(k+1)} - \phi_{(i+1)(j)(k-1)} - \phi_{(i-1)(j)(k+1)} + \phi_{(i-1)(j)(k-1)},\\
\frac{\partial^2\phi}{\partial\xi_2\partial\xi_3} &= \phi_{(i)(j+1)(k+1)} - \phi_{(i)(j-1)(k+1)} - \phi_{(i)(j+1)(k-1)} + \phi_{(i)(j-1)(k-1)}.
\end{aligned} \tag{3.29}$$

To calculate the metric tensors, the base vectors must also be approximated numerically. The base vectors are the first-order spatial partial derivatives and the quadratic template is used for the approximation in the same manner as that used for the solution variable, ϕ. The second derivatives of the basis functions are the first derivatives of the base vectors and they are used to generate the base vector derivatives, Γ (equation (3.23)).

Implicit and explicit formulations

The transmembrane potential (V_m) equation contains a time derivative that can be approximated by a first-order forward time approximation

$$\frac{\partial V_m}{\partial t} = \frac{V_m^{t+\Delta t} - V_m^t}{\Delta t}. \tag{3.30}$$

We present two methods to add the discrete form of the time derivative to the bidomain or monodomain models, giving explicit and implicit formulations. If the two bidomain diffusion terms are represented by I_{V_m} and I_{ϕ_e}, the transmembrane equation can be written

$$I_{V_m} + I_{\phi_e} = A_m\left(C_m\frac{V_m^{t+\Delta t} - V_m^t}{\Delta t} + I_{\text{ion}}^t\right) - I_{s2}^t. \tag{3.31}$$

The explicit formulation is created by setting the time of I_{V_m} to be t and the update for the transmembrane potential is then

$$V_m^{t+\Delta t} = V_m^t + \frac{\Delta t}{A_m C_m}\big(I_{V_m}^t + I_{\phi_e}^t + I_{s2}^t\big) - \frac{\Delta t}{C_m}I_{\text{ion}}^t. \tag{3.32}$$

For each FD node, the group of points used to create the local quadratic element are stored along with the corresponding diffusion coefficients. This allows the evaluation of the two diffusion terms to be reduced to two inner products of the stored coefficients with the appropriate potential values – one inner product for the I_{V_m} term and one for the I_{ϕ_e} term.

The implicit formulation uses I_{V_m} based at the new $t + \Delta t$ time-step, and is given by

$$V_m^{t+\Delta t} - \frac{\Delta t}{A_m C_m} I_{V_m}^{t+\Delta t} = V_m^t + \frac{\Delta t}{A_m C_m}\left(I_{\phi_e}^t + I_{s2}^t\right) - \frac{\Delta t}{C_m} I_{\text{ion}}^t. \tag{3.33}$$

The left-hand side of this equation is written into a matrix system where one row is generated for each FD point, and the column positions correspond to the difference point numbers that define the local quadratic element.

Numerical and computational issues

The wave of electrical activation travels through cardiac tissue with a very steep wavefront owing to the fast response of ventricular cells to electrical stimulation (the rapid upstroke of the cellular action potential, as will be described in Section 4 – see Figure 4.3). This leads to high spatial gradients of electrical potential in the region around the wavefront, requiring the use of a very high-density finite difference grid to resolve the wavefront accurately. Ahead of the wavefront and behind the activation wave, however, tissue is inactive and recovering, respectively, and a lower-density grid is sufficient to resolve the slower electrical activity. Therefore the use of a uniformly high-resolution finite difference grid results in a large computational overhead for the inactive and recovering regions of tissue. Adaptive grid techniques are well suited to this type of problem, where only the region of tissue about the activation wavefront is solved using the high-resolution grid, while inactive regions use lower-resolution meshes and recovering regions use a medium-density mesh. Currently we are testing an implementation of a multigrid technique (McCormick 1989) which allows for the specification of multiple grid *levels*, with stepping between these levels during model simulation.

Numerical solution of the electrical activation model requires two steps: integration of a system of ordinary differential equations for the cellular processes at each point to calculate I_{ion} and solution of the bidomain equations (3.14)–(3.15) or monodomain model (3.19) for V_m. Using anything other than the simplest cellular models, this first step will have significantly greater computational demands than the solution of the advection–diffusion equation. This is also a target for parallelization. The cellular ODEs at each grid point can be integrated independently for a given time-step, suggesting that this integration is an ideal candidate for multiprocessing. Given no communication between grid points during a time-step the integration of the cell model should scale linearly with the number of processors in a

shared memory system, while the communication between the cellular and continuum models represents a fixed cost which restricts the scalability on distributed memory systems.

3.3. Coupled electro-mechanics

In the previous sections, we have seen how a finite element model of finite deformation elasticity can be formulated, and the same finite element description can be used to model the spread of electrical excitation. Previous work (Hunter, Nash and Sands 1997) has modelled the electrical excitation and mechanical contraction as two separate processes weakly coupled together through the use of the excitation wavefront to initiate active contraction of the tissue. However, in cardiac tissue these two processes are tightly coupled at both the cellular and tissue levels and essential physiology is left out of such weak-coupling models. Not only does the electrical excitation initiate mechanical contraction but mechanical deformation alters the electrophysiology at both the tissue and cellular levels. The cellular level models described in Section 4 describe these effects in cell models; here we concentrate on the continuum tissue level models.

The collocation technique introduced in the previous section allows macroscopic changes in electrical activation processes due to the mechanical deformation of the tissue. Active contraction of muscle fibres generates force only in the direction of the fibre axis (aligned with the ν_1-coordinate). Therefore only one term from the stress tensor needs to be modified, and so if the stress tensor is expressed with respect to the microstructural material axes, only the T^{11} component is modified:

$$T^{\alpha\beta} = \frac{1}{2}\left(\frac{\partial W}{\partial E_{\alpha\beta}} + \frac{\partial W}{\partial E_{\beta\alpha}}\right) - p a^{\alpha\beta}_{(\nu)} + T a^{11}\delta^{\alpha}_{1}\delta^{\beta}_{1}, \tag{3.34}$$

where $T = T(t, \lambda_{11}, \ldots)$ is the active tension generated by a fibre at time t. The fibre extension ratio, $\lambda_{11} = \sqrt{2E_{11} + 1}$, defines the current stretch or compression at a given collocation grid point and is determined from a cellular model discussed in Section 4. The value of the active tension at a given Gauss point in the finite element scheme will be defined by the cellular model parameters interpolated from the nearest neighbour collocation grid points, with the collocation points closest to the Gauss point having greater influence than those distant to it. Given the finite element description of strain in the tissue model, the fibre axis strain is readily estimated, and hence the extension ratio can be calculated at any grid point.

Numerical simulation

Although the electrical excitation and mechanical contraction are physiologically interdependent, the quasi-static techniques used for the solution of

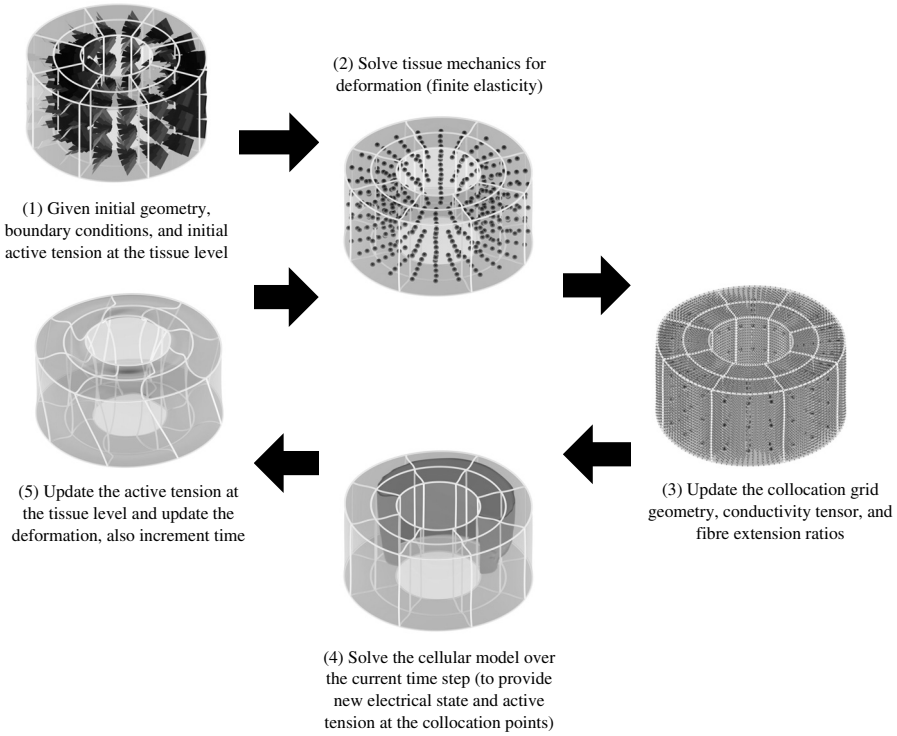

Figure 3.3. Schematic illustration of the iterative solution process for coupled cardiac electromechanics simulations of continuum tissue models. (See text for more detail.)

the finite elasticity tissue models and the fact that the electrical and cellular processes take place on much faster time-scales allows for some uncoupling in the continuum model simulation. Figure 3.3 highlights the algorithm used for the solution of coupled electromechanics in continuum tissue models. This algorithm allows for the independent solution of the finite elasticity and electrical propagation models at a given instant in time, resulting in two solution steps separated by an update step in which information is either transferred from the FE nodes to the FD grid points or *vice versa*.

Any simulation starts with a description of the model and some initial conditions. In this case the model definition includes a finite element geometry (including the fibrous microstructure continuum representation), the constitutive material law for the mechanical model, the continuum material parameters, and specification of the cellular model. The simulation framework developed allows for spatial variation of cellular models and parameters within models. Initial conditions required for solution of the finite deformation elasticity and electrical activation are covered in the previous sections.

Given an initial state for the tissue, an iteration of the finite element algorithm can be performed to give the deformed geometry at time t.

After mechanical deformation of the finite element geometry the location of the collocation points remains unchanged in solution space, but their global position and microstructural axes need to be updated. The metric tensors (equation (3.22)) and the effective conductivity tensor (equation (3.25)) are also updated before the diffusion coefficients (equation (3.21)) are recomputed. The extension ratio values at the collocation grid points are updated by interpolation of the finite element strain field.

With the collocation grid points updated, the cellular models can be integrated forward by one time-step from time t to $t+\Delta t$ and the bidomain equations solved to determine the spread of activation. The size of the time-step (Δt) can be significantly larger than the actual integration time-step required for a converged integration of the cellular differential equations and the bidomain equations. This is due to the much shorter time-scales for kinetics of the cellular level models and the propagation of electrical activation compared to the mechanical contraction. As an indication, the time-step typically required for integration of the the bidomain equations is on the order of 0.01 ms while the mechanics can typically be updated and recomputed on the order of 1.0 ms. The cellular models may require even finer time resolution, which can be accomplished with the use of adaptive time-stepping ODE integrators within a bidomain model time-step (*e.g.*, LSODA (Hindmarsh 1983)).

The solution of a time-step in the cellular model produces a new value for the active tension T at each collocation point. This active tension is then interpolated from the collocation grid points back to the finite element Gauss points as described. With the new active tension values the finite deformation elasticity model can be solved anew, resulting in the deformed geometry at time $t + \Delta t$.

4. Cellular modelling

The mechanisms by which tissue contracts in response to electrical stimulation, consuming energy provided by metabolism in the process, reflect events taking place at the sub-cellular level, and thus necessitate modelling at much smaller spatial scales from those outlined above. For continuum scale investigations of tissue and whole organ function, cellular processes may be included in simulations using simple empirical representations, in some instances using only a single variable, for example, to represent active tension, or the state of electrical activation (via the I_{ion} current term in equation (3.15)). However, a detailed mathematical quantification of the subcellular biochemistry is necessary to couple the activity of processes

operating across the range of spatial scales of organization that are characteristic of complex organs such as the heart, for example, to study the effects of pharmaceutical interventions on pump function. Heart cells, like any other cell, are hugely complicated, highly organized and regulated entities. Therefore, cellular models are typically developed with the competing demands of biophysical accuracy and computational simplicity. This challenge has not entirely been met. While progress in the key areas of electrical activation and cellular mechanics has led to highly sophisticated models, which we outline below, the energetics component of cellular physiology has largely been neglected until very recently, and a satisfactory framework for coarse graining and averaging cell properties for incorporation into tissue and organ simulations is yet to emerge. It is clear that such approximation techniques must be developed in order to make fully coupled simulation of the heart, with some 10^9 cells, computationally tractable.

4.1. Active tension development

Heart tissue is made up of sheets of muscle fibres, myofibres, bound together with connective tissue, as discussed in Section 1.1. Myofibres comprise muscle cells, myocytes, which contract in response to electrical stimulation. Inside these striated muscle cells are myofibrils, bundles of contractile proteins, which can be resolved into sarcomeres, the repeating structural elements which are the functional contractile units of the cell. Sarcomeres consist of parallel and overlapping filaments of actin and myosin protein, organized into a regular cross-sectional lattice, in which a hexagonal array of thin actin filaments surrounds each thick myosin filament (see Figure 4.1). The molecular mechanism which generates active tension is due to the interaction of these proteins. Projections from the thick myosin filaments attach to thin actin filaments to form tension-bearing cross-bridges. These cross-bridges form, undergo conformational change to a load-bearing state, dissociate and reattach in a cycle to propel the thick filaments past the thin filaments, shortening the sarcomere and contracting the cell.

This process takes place in response to electrical activation via a sequence of events in the cell. Calcium ions are required to trigger active contraction. At rest, the intracellular concentration of calcium is maintained at very low levels. One of the consequences of activation of the cell is that calcium ions enter through the cell membrane. This small influx of calcium however triggers much larger release from storage sites within the cell, in a high-gain process known as calcium-induced calcium release. Calcium ions must bind to the muscle fibres in order to allow cross-bridges between the thick and thin filaments to be formed. Therefore the contraction is dependent on the calcium level in the cell. However, calcium ions are actively removed from inside the cell, both via re-uptake into the intracellular calcium stores,

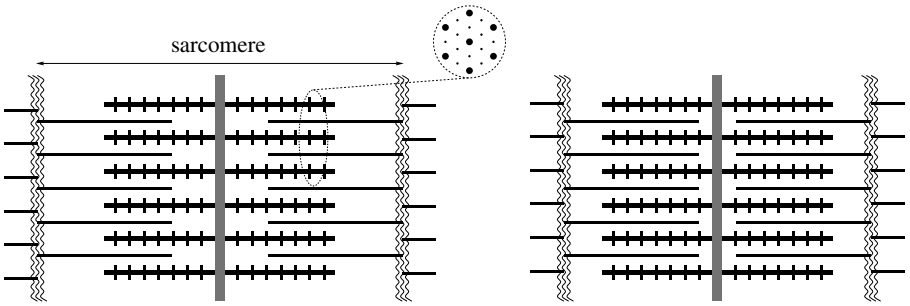

(a) Diastole (relaxed) (b) Systole (contracted)

Figure 4.1. Schematic illustration of the overlapping thick (myosin) and thin (actin) filaments of a sarcomere, viewed along its length. (a) shows the relaxed sarcomere, and (b) the sarcomere in a state of contraction, where the thick and thin filaments have moved past each other due to the action of cross-bridges (here the myosin heads are represented as spurs protruding from the thick filaments). In (a) the cross-sectional organization of the filaments is represented (inset).

where it is unavailable to the muscle fibres, and by extrusion from the cell itself. As a result the level of calcium in the cell is only transiently raised following electrical activation, and so the tension development follows the same periodicity as the electrical stimuli received by the cell.

Models of active force generation in cardiac muscle can therefore be developed in three parts: (i) the calcium transient and calcium binding to the thin filaments, (ii) the availability of thin filament binding sites for cross-bridges to form, and (iii) the kinetics of actin-myosin cross-bridges themselves. Calcium binding to accessory proteins (Troponin-C) is a saturating function of the calcium concentration [Ca],

$$[\text{Ca-TnC}] = \frac{\alpha\,[\text{Ca}]}{[\text{Ca}] + \beta(T)}, \tag{4.1}$$

where [Ca-TnC] is the concentration of Ca-bound Troponin-C (TnC) and $\beta(\cdot)$, the rate of unbinding from TnC, is a decreasing function of the developed tension T. As a result of calcium binding to TnC, a sequence of events is initiated which results in the conformational change of a protein complex, removing a physical obstruction to formation of the actin-myosin cross-bridges. The kinetics of this process are essentially governed by a

first-order equation of the form

$$\frac{\mathrm{d}z}{\mathrm{d}t} = f\big([\text{Ca-TnC}]\big)(1-z) - bz, \tag{4.2}$$

where the variable z represents the fraction of actin binding sites available for cross-bridge formation and the rate at which sites become available $f(\cdot)$ is an increasing function of the [Ca-TnC] complex, and hence of calcium concentration and developed tension.

The steady state tension developed in muscle fibres has long been known to depend on the length of the muscle. This property in heart tissue (Guz, Bergel and Brutsaert 1974) reflects that greater tension and hence pumping capacity is generated in the heart when distended, *i.e.*, with increased extension of the myofilaments. The steady-state tension T_o at a given calcium concentration is linearly dependent on both sarcomere length, λ, and the available fraction of actin binding sites, z:

$$T_o \propto \big(1 + \beta_0\,(\lambda - 1)\big)z, \tag{4.3}$$

where β_0 is the slope of the linear tension-length relation.

Actin–myosin cross-bridge kinetics

Cross-bridge kinetics, first modelled by Huxley (1957), are the result of transitions between attached force-bearing configurations, and non-force-bearing unattached states of the actin-myosin cross-bridges within each myocyte. The rates of transition between each state are dependent on the strain carried by a given cross-bridge head, and the concentrations of metabolite molecules such as ATP (Adenosine Tri-Phosphate) whose chemical free energy of hydrolysis is converted to work via the cross-bridge cycle. At the level of a single cross-bridge, the time-dependence of transition rates on cross-bridge strain x, the extension of the myosin head when attached to an actin binding site, requires the system be modelled as a system of partial differential equations (Huxley 1957, Hill 1975). The conservation laws for cross-bridges which can be in one of n biochemically or mechanically distinguished states with probability $p_i(x,t)$, with muscle shortening velocity $v(t)$, are given by

$$\frac{\partial p_i}{\partial t} - v(t)\frac{\partial p_i}{\partial x} = \sum_{\substack{j=1\\ j\neq i}}^{n} p_j(x,t)\alpha_{ji}(x) - p_i \sum_{\substack{j=1\\ j\neq i}}^{n} \alpha_{ij}(x), \tag{4.4}$$

where α_{ij} is the transition rate between the ith and jth states, which may depend on the cross-bridge strain x (for transitions between unattached and attached states, or for a change of conformation between two attached states, where chemical energy from ATP is used to change the protein conformation and increase the strain in the cross-bridge). In practice it is

usually assumed that kinetics are restricted to a cycle, the cross-bridge cycle, and so the rates of transition between non-adjacent states in the cycle are zero. Conservation of the total number of cross-bridges leads to a system of $n-1$ coupled first-order hyperbolic PDEs, along with the relation

$$p_n(x,t) = 1 - \sum_{i=1}^{n-1} p_i(x,t). \tag{4.5}$$

Typically in this model cross-bridges are assumed to be independent force-generating elements, and also it is assumed that strain x is a continuous variable. In fact, myosin heads and actin binding sites are discretely spaced, but in the limit of large numbers for averages taken over large populations of cross-bridges this is a reasonable approximation. Furthermore, cooperative interactions between cross-bridges have been suggested to explain some muscle data, in particular the steady state force-calcium curve, which shows a sigmoidal-type relationship between the tension generated and the concentration of calcium ions (Rice and de Tombe 2004).

Huxley considered a two-state model, with one attached and one unattached state, which reduces to a single first-order hyperbolic PDE. For suitably chosen piecewise linear functions for attachment and detachment rates this model can be solved analytically, for example, to produce steady state distributions of attached cross-bridges for different contraction velocities v. More complicated models have been proposed which include numerous states, reflecting changing views about the detailed biochemistry underlying the cross-bridge cycle (Piazzesi and Lombardi 1995, Smith 1998). Hill has shown from principles of chemical free energy transduction that the strain-dependent transition rates for these models are not in fact independent of one another, as their ratios are related to the free energy change associated with the transition, which must also reflect the change in energy associated with the change in cross-bridge strain (Hill 1975, 1989). Typically this is calculated by assuming that each cross-bridge functions as an elastic element which develops tension $k(x)$ which is a function of its displacement from the actin binding site. The tension generated in a population of cross-bridges is calculated by integrating over the distributions of tension-bearing states (assuming uniform distribution of cross-bridges along filaments and hence uniform probability of strain x)

$$T(t) = \int_{-\infty}^{\infty} k(x) \left[\sum_{j_{\text{att}}} p_j(x,t) \right] \mathrm{d}x, \tag{4.6}$$

where the sum is over attached cross-bridge states and $k(x)$ is the force developed by a cross-bridge at strain x. Often it is assumed that the

myosin heads are linear elastic elements, in which case the tension developed per sarcomere is proportional to the first moment of the distributions, summed over attached states.

Averaging and empirical modelling

For solving continuum-scale tissue mechanics problems, the active tension generated by cellular contraction is required at a large number of spatially distributed points in the model. Solving systems of partial differential equations at each point is computationally prohibitive in this context. However, to accurately model contraction, and in particular the energetics of this process in tissue we need to retain many details from this molecular description of the contractile apparatus. Two suggestions have been made for tissue level simulations. Zahalak has proposed that ODE approximations for the zeroth, first and second moments of the PDEs can be made if it is assumed that the distributions of attached and unattached states with strain are Gaussian in form (Zahalak 1981). It is a well-known property of the normal distribution that the first three moments can be expressed in closed form in terms of each other. This approach has been proposed for both skeletal (Zahalak 1981, Zahalak and Ma 1990) and cardiac cells (Guccione, Motabarzadeh and Zahalak 1998). The validity of the assumption of normal distributions is questionable, however, particularly for perturbations away from isometric (*i.e.*, zero velocity) equilibrium. An alternative view of this problem is to produce an empirical model of tension development in muscle cells which can be related back to molecular processes.

The model of Hunter *et al.* (Bergel and Hunter 1979, Hunter 1995, Hunter, McCulloch and ter Keurs 1998) couples a linear time-dependent component for contraction with a static nonlinearity to produce a phenomenological description of tension development associated with cross-bridge kinetics:

$$\frac{T}{T_o} = \frac{1 + aQ(v)}{1 - Q(v)}, \tag{4.7}$$

where a is a parameter fitted from the steady state tension-velocity relationship and T_o is the steady state isometric (zero velocity) tension (see equation (4.3)). $Q(v)$ is a linear response function of the shortening velocity $v(t)$ with m components, which can be represented as an hereditary time integral or *fading memory* model

$$Q = \sum_{i=1}^{m} Q_i = \sum_{i=1}^{m} A_i \int_{-\infty}^{t} \mathrm{e}^{-\alpha_i(t-\tau)} v(\tau)\,\mathrm{d}\tau, \tag{4.8}$$

and the parameters A_i and α_i can be recovered from data on studies of muscle stiffness measured for transient length and force-step experiments,

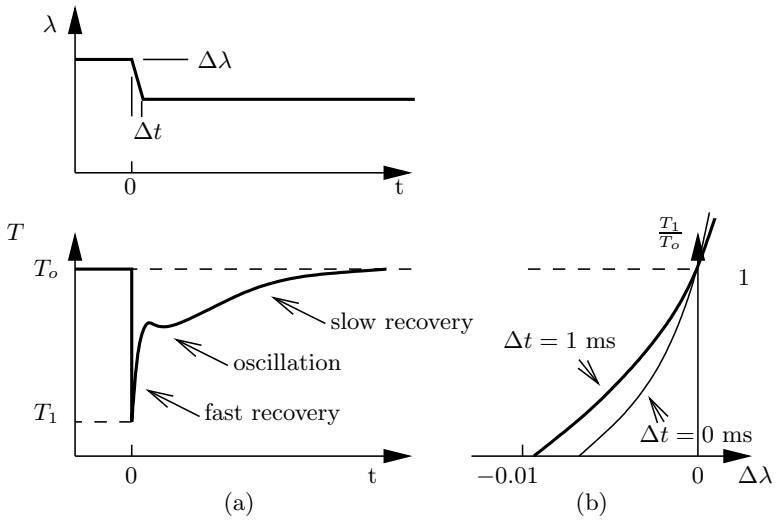

Figure 4.2. (a) Tension recovery (lower figure) following a length step of $\Delta\lambda$ of duration Δt (upper figure). Notice the different phases of the tension recovery. (b) Tension T_1 reached at the end of the length step, divided by isometric tension T_o, plotted against the magnitude of the length step $\Delta\lambda$. One curve is for a length step of 1 ms duration and the other for an idealized instantaneous step.

and for sinusoidal length perturbations about equilibrium over a range of frequencies, for both skeletal (Kawai and Brandt 1980, Kawai, Zhao and Halvorson 1993*b*) and cardiac (Saeki, Kawai and Zhao 1991) preparations. The form of this fading memory component is equivalent to the transfer function fitted from these sinusoidal perturbation data, and typically for cardiac muscle it is determined that three components are required to describe the response of tissue.

The model captures many features of real muscle experiments, for example the tension developed following a step change in muscle length, shown schematically in Figure 4.2. Furthermore, the dependence of the parameters of the fading memory model on metabolites such as ATP can be characterized from experimental data (Saeki *et al.* 1991, Kawai, Saeki and Zhao 1993*a*), and this is necessary in order to couple the active tension generation to models of energy metabolism in the cell. However, with this type of model a calculation of the energetic cost of contraction is not readily accessible, as the link to the molecular mechanisms of contraction

is not included in the fading memory framework. The links between these two modelling approaches and the underlying cross-bridge theory of Huxley have recently been investigated and discussed by Smith (2003).

Computational efficiency of the fading memory model

In the context of tissue and organ scale mechanical simulations, the computational efficiency of cell models is critical. The properties of the exponential decay term allow the tension at a new time $(t + \Delta t)$ to be written in terms of the length history up to time t weighted by the decay over Δt, together with the hereditary integral contribution from the latest time increment Δt:

$$Q_i(t + \Delta t) = \mathrm{e}^{-\alpha_i \Delta t}\left[Q_i(t) + A_i \int_t^{t+\Delta t} \mathrm{e}^{-\alpha_i (t-\tau)} v(\tau)\, \mathrm{d}\tau\right]. \tag{4.9}$$

The Q_i are then summed as in equation (4.8) to yield a solution for current active tension T. This provides an efficient method for calculating the time-dependent generation of active tension at the large number of Gauss points in a finite element mesh required to geometrically represent cardiac tissue and organ models.

4.2. Cellular electrophysiology

Contraction of the heart is triggered by a wave of electrical excitation moving through the tissue. This travelling wave is generated by the rapid depolarization of the cell membranes of the muscle cells (myocytes) from a negative resting potential, called an action potential. Muscle cells are for the most part electrically excitable. The resting potential is a stable steady state, and small displacements quickly decay back to rest. However, a super-threshold stimulus generates a large-amplitude trajectory, the action potential, before the membrane potential returns to its resting value. This response to a sufficiently large stimulation is at the basis of the electrical properties of heart muscle.

The electrophysiological properties underlying excitability were first understood in a mathematical model of a nerve cell, the squid giant axon, due to Hodgkin and Huxley (1952). As for other electrically excitable tissues, the active constituent of nerve cells and heart cells is the membrane (sarcolemma) which isolates the contents of a cell from its external environment. Electrical excitability in transmembrane potential is a consequence of the processes controlling the transport of electrically charged species across the cell membrane. This membrane is selectively permeable to charged ionic species, such as sodium, potassium and calcium ions. The passage of ions through the cell membrane is regulated by ion-specific pores, or ion chan-

nels, whose permeability may be controlled by the cell membrane electrical potential (voltage-gating) or by the binding of other ions or metabolites. The different properties of two such voltage-gated ion channels, controlling the flux of sodium and potassium ions, were sufficient to explain the excitability in the squid giant axon.

Ion channels and voltage gating

The opening and closing of ion channels in response to changes in potential underlies the excitability of the membrane. When an ion channel is open, the direction in which ions move through the channel is dictated by the electrical and chemical gradients which they experience. Ions move down a concentration gradient until the motive force is balanced by the opposing electrostatic force, produced by the potential difference across the membrane due to net movement of charge. The distribution of each ionic species on either side of the membrane determines a membrane potential, the Nernst potential, at which there is zero net motive force, for the ith ion, V_i. In many cell types including cardiac myocytes the resting potential, at which the voltage-dependent sodium channels are predominantly closed, is close to the Nernst potential for potassium.

Current balance for the capacitive membrane gives a differential equation for the membrane potential of the form (Hodgkin and Huxley 1952, Keener and Sneyd 1998)

$$C_m \frac{\mathrm{d}V_m}{\mathrm{d}t} = -\sum_i g_i x_i^n y_i^m (V_m - V_i) + I_s, \tag{4.10}$$

where the sum over subscript i is over the range of different types of ion channels in the membrane. The gating variables x_i and y_i describe, respectively, the activation (opening) and inactivation (closing) of channels, taking values between 0 and 1, according to the differential equations

$$\tau_{x_i}(V_m) \frac{\mathrm{d}x_i}{\mathrm{d}t} = x_i^\infty(V_m) - x_i \tag{4.11}$$

and a similar equation holds for y_i. The relaxation time-scale $\tau_{x_i}(V_m)$ and steady state value $x_i^\infty(V_m)$ are functions of the membrane potential (for voltage-gated channels). Parameters n and m reflect the number of independent gating subunits of each type making up the ion channel, which must all be in an open state for the passage of ions. The conductance g_i for the ith channel is for the open channel, and C_m is the capacitance of the membrane. I_s represents a current source applied to the cell, for example the initial stimulus from neighbouring cells. This framework is at the root of all contemporary models of cellular electrophysiology (Miura 2002).

Hodgkin and Huxley also studied the propagation of the action potential in a simple spatially extended version of their model using cable theory.

They were able to calculate the speed of the travelling wave along the axon of the nerve cell using the shooting method, in 1952, on a manually cranked calculator (a Brunsviga 20), due to the labours of Andrew Huxley (Hodgkin 1976).

Electrical excitability in the heart

The physiological principles which underlie excitability in the heart are essentially the same as for any other excitable cell type. In some cases simplified models can be produced and separation of time-scales used to reduce the complexity of a model (see, for example, Smith and Crampin (2004)). On the other hand, there are many processes involved in generating and regulating the electrical properties of cells. For example, more than 20 different types of ion channel have been identified in the myocyte. The same modelling framework can be expanded by the addition of equations representing the active (energy-requiring) transport of ions against their electrochemical gradients by ion pumps and exchangers in the membrane, which are required to maintain the resting state of the cell and to regulate cell calcium. One important feature of the cardiac action potential is that it has a so-called plateau phase during repolarization back to the resting potential, during which calcium ions enter the cell triggering a larger release from intracellular calcium stores (see Figure 4.3). This calcium-induced calcium release initiates the contraction of the muscle filaments, as discussed above. Equations describing these processes can be incorporated to produce comprehensive models of cellular electrophysiology.

The most extensive of these cardiac models are the ion channel models pioneered by Noble and co-workers (Noble 1960, DiFrancesco and Noble 1985, Noble *et al.* 1998), and the Luo and Rudy models (Luo and Rudy 1991, 1994), focusing on the physiological behaviours of premature stimulation and arrhythmogenic activity of the single myocyte. Their model has since been extended by Jafri, Rice and Winslow (1998), among others, to accommodate more complex calcium kinetics which are important for contraction coupling, as discussed above. One important consideration that is introduced by more realistic models of calcium handling is that the cellular compartment into which calcium channels empty (the diadic space) is very small, and furthermore the release of calcium from the internal stores has been shown to be in discrete quantities, or sparks, introducing very short time-scales and a stochastic element to cell models, which may be important in some circumstances (Greenstein and Winslow 2002).

4.3. Metabolic models

Muscle cells convert metabolic (chemical) energy to work via a sequence of biochemical processes involving the breakdown (or hydrolysis) of the

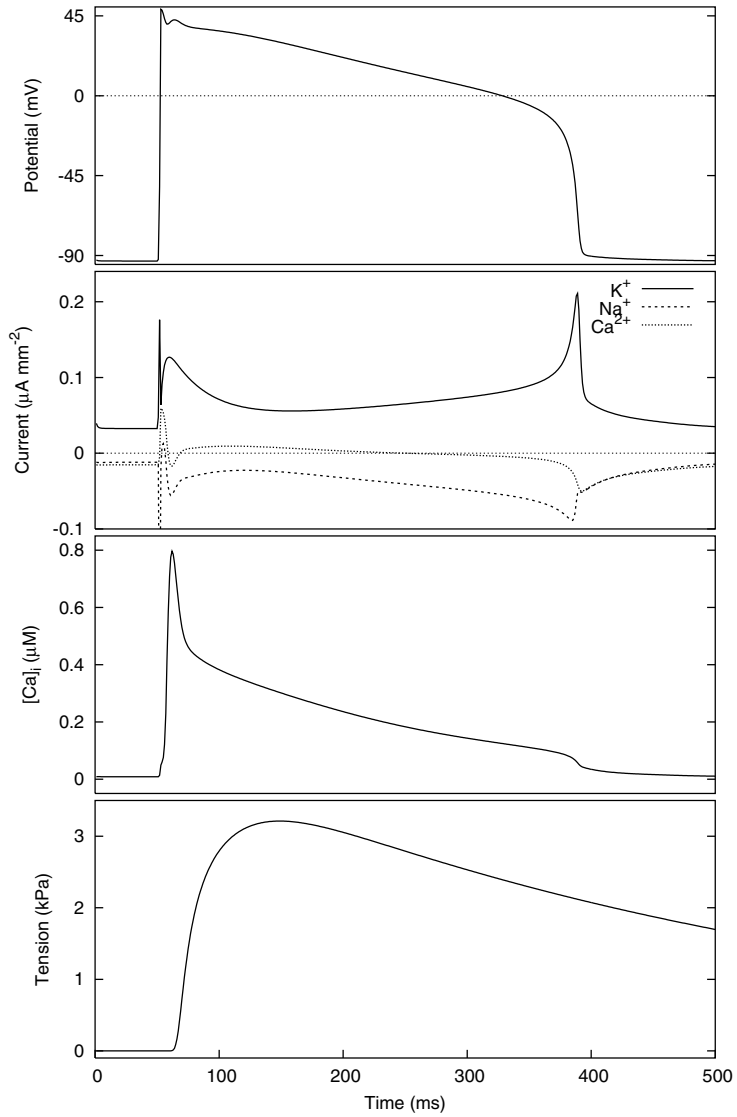

Figure 4.3. Figure showing, from top to bottom, ventricular action potential, ionic currents, intracellular calcium transient and active tension development from a cardiac myocyte model. Note that the rapid inward (negative) component of the sodium current (Na^+; dashed line), which initiates the action potential upstroke, reaches a much greater maximal amplitude than is shown in the figure (where the scale is truncated at $-0.1\mu\text{Amm}^{-2}$). These traces were generated using the ventricular electrophysiology model of Noble *et al.* (1998) coupled to the HMT mechanics model of Hunter *et al.*, as described in Nickerson, Smith and Hunter (2001).

molecule ATP (Adenosine Tri-Phosphate). Energy-requiring reactions, for example muscle contraction due to the kinetics of binding and unbinding of actin–myosin cross-bridges, and transmembrane ion pumps operating against an electrochemical gradient, are coupled to the hydrolysis of ATP which releases energy. As might be expected, there is an intricate feedback of energy demand to supply in the cell, particularly acting at the major sites of ATP generation in the cell, the mitochondria, where ATP is formed by the process of respiration, using oxygen from the blood (Nicholls and Ferguson 2002).

Despite its importance to heart function, metabolism has received less attention for quantitative models of the heart. It is fair to say that the major attention in cell modelling has been on cell electrophysiology. This is perhaps natural, both because of its obvious centrality in understanding the electrical activation of cardiac cells and the initiation of contraction, but also probably because of the development of sensitive experimental techniques for recording cell membrane voltages and transmembrane ion currents. (The patch-clamp technique and its many progeny use micropipette electrodes coupled with high-impedance amplifiers to measure transmembrane currents from individual ion channels.) However, nuclear magnetic resonance (NMR) techniques can now be used to monitor metabolite concentrations in the beating heart, and increasingly data is becoming available which allows for the development of more sophisticated metabolism models as components for whole-cell modelling. To study the normal function of organs such as the heart, electrophysiology and contraction can be characterized, and models parametrized, for normal metabolic conditions, where the heart is well perfused with an oxygenated blood supply through the microcirculation. However, of very significant interest is the use of the modelling framework described in this article to understand dysfunction in the heart, and in particular dysfunction caused by ischaemic heart disease. Ischaemia is the reduction or loss of blood supply to the heart, or a region of the heart muscle (Opie 1998). There may be many underlying clinical reasons for ischaemic episodes, by which the coronary flow is reduced, however, the major effect on the cells is disruption of the balance of supply and demand for ATP, resulting both from the reduction in oxygen supply and from the reduction in blood flow to transport energy substrates to, and waste products from the cells.

The result of ischaemia on the muscle is an increase in the acidity of the cells (acidosis), changes to the distribution of ionic species across the cell membrane, which affect the electrophysiological properties of the cells, and eventually the loss of ATP to drive energy-requiring reactions. The final consequence of these disturbances is the loss of the contraction cycle, pump failure and cell death (infarction). However, before this occurs the

changes to the ionic milieu can also give rise to pathological electrical behaviours, or arrhythmias. The origins of these arrhythmogenic processes are not well understood, and detailed cell and tissue modelling provides a testbed for different theories and potential therapies. ATP and its hydrolysis products, and in particular the cell acidity levels, regulate many of the electrophysiological and calcium handling processes in the cell. This network of regulatory interactions is now being incorporated into detailed cell models for the heart. The additional complexity of accounting for metabolites and acidity notwithstanding; the major difficulty again with numerical simulations involving metabolism is the inclusion of processes which take place over time-scales of minutes to hours, *i.e.*, many heart beats, rather than the millisecond time-scales of most electrophysiological processes. Furthermore, the loss of blood supply is usually localized to one region of the muscle, with a gradation of effects moving laterally away from the fully ischaemic zone. The resulting spatial heterogeneity of cell properties is thought to be strongly influential in the developing pathophysiology, and is a significant further challenge to modelling studies. A description of continuum modelling approaches for the coronary vasculature and microcirculation blood supply to the heart is presented in Section 5.

Computational and modelling issues

These models of cellular electrophysiology and metabolism are described by coupled systems of nonlinear ordinary differential equations, possibly with the addition of stochastic components for certain ion channel gating and calcium handling processes. An essential characteristic of these components for integrated modelling of physiological systems is the wide range of time-scales that are introduced. For example, the upstroke of the action potential takes place on the sub-millisecond time-scale, whereas the duration of the cardiac action potential itself is on the order of several tenths of a second. The introduction of metabolic processes into cell models introduces components with time constants of seconds and longer – several orders of magnitude larger than the (sub-) millisecond electrophysiological time-scales. This gives rise to large stiff systems of coupled ODEs to describe the kinetics of the various processes which underlie the action potential and its regulation by metabolism. While numerical simulation over this range of time-scales for a single cell presents few difficulties for modern computers, the coupling of large numbers of cells in a continuum tissue framework represents a significant hurdle to simulation studies (there are 10^9 or so cells in the human heart). Faster algorithms for very stiff ODE systems, along with refinements in modelling which allow course graining or adiabatic approximations for slowly varying properties are therefore needed.

5. Vascular blood flow

A third important continuum element of tissue models, following mechanical and electrical activation, is representation of the network of coronary blood vessels (vasculature) which supply cardiac tissue with oxygenated blood. The spatio-temporal distribution of the supply of oxygen and metabolic substrates (perfusion) is an important determinant of heart function, typically via its influence on the state of cellular metabolism (models of which were introduced in Section 4.3). Interactions between vascular perfusion and organ function are also relevant at the continuum modelling scale.

The arterial and venous vessels are elastic tubes, and so their volume is a function of the difference between the blood pressure and the mechanical state of the tissue in which the vessels are embedded. Thus the vascular fluid dynamics are integrally coupled to tension generation and deformation of the tissue.

Several recent studies have used statistical morphometric data to reconstruct vascular network geometries using measurements from casts (Kassab *et al.* 1993, Kassab and Fung 1994), image segmentation (Kantor *et al.* 1999) and spatial distributing algorithms (Smith, Pullan and Hunter 2000). These geometries provide the foundation for an anatomically based model of vascular blood flow. Computational limitations motivate the reduction of the full Navier–Stokes equations to produce a one-dimensional model of flow in a single vessel segment, which we describe below. The use of constraints to maintain conservation relations across bifurcations in the branching network is introduced (in Section 5.2). A lumped parameter model (Section 5.3) is used to represent small vessel microcirculation networks distributed at fine spatial resolution. Finally, modelling the effect of tension generation and deformation on blood flow in the coronary network is described in Section 5.4.

5.1. Single vessel model

There are a number of fundamental assumptions about vascular blood flow used in deriving the governing equations for the model presented here. The studies of Perktold, Resch and Peter (1991) and Cho and Kensey (1991) indicate that the shear thinning properties of blood do not play a significant role in large diameter vessels. This is because the relative size of red blood cells to vessel diameter is small and therefore blood can be modelled as a continuum. The distensibility of a coronary vessel wall is assumed to dominate any effects due to the compressibility of blood. Thus, in the equations below, blood is modelled as an incompressible, homogeneous, Newtonian fluid. The low Reynolds number applicable to the majority of the circulation means that all flows are assumed to be laminar.

With these assumptions the Navier–Stokes equations can be expressed using a cylindrical coordinate system (r, θ, x), where the x axis is aligned

with the local vessel axial direction. Assuming velocity in the circumferential direction is zero and that the flow is axi-symmetric, the equations governing fluid flow reduce to

$$\frac{\partial v_x}{\partial t} + v_r\frac{\partial v_x}{\partial r} + v_x\frac{\partial v_x}{\partial x} + \frac{1}{\rho}\frac{\partial p}{\partial x} = \nu\left(\frac{\partial^2 v_x}{\partial r^2} + \frac{1}{r}\frac{\partial v_x}{\partial r} + \frac{\partial^2 v_x}{\partial x^2}\right), \tag{5.1}$$

$$\frac{\partial v_r}{\partial t} + v_r\frac{\partial v_r}{\partial r} + v_x\frac{\partial v_r}{\partial x} + \frac{1}{\rho}\frac{\partial p}{\partial r} = \nu\left(\frac{\partial^2 v_r}{\partial r^2} + \frac{1}{r}\frac{\partial v_r}{\partial r} - \frac{v_r}{r^2} + \frac{\partial^2 v_r}{\partial x^2}\right). \tag{5.2}$$

In these equations $v_x(x,r)$ and $v_r(x,r)$ are the axial and radial velocities. Pressure, viscosity and density are denoted by $p(x)$, ν and ρ respectively. Conservation of mass is governed by

$$\frac{\partial v_x}{\partial x} + \frac{1}{r}\frac{\partial\,(r v_r)}{\partial r} = 0. \tag{5.3}$$

We make the further assumption that radial velocity is small compared to axial velocity and, consistent with experimental observation, that the radial velocity profile can be represented in the form

$$v_x = \frac{\gamma+2}{\gamma}V\left[1 - \left(\frac{r}{R}\right)^{\gamma}\right], \tag{5.4}$$

where $V(x)$ is average flow velocity, $R(x)$ is the internal vessel radius and γ is an empirical fitting parameter (Smith, Pullan and Hunter 2002).

Equations (5.1)–(5.3) can be reduced such that conservation of mass is governed by

$$\frac{\partial R}{\partial t} + V\frac{\partial R}{\partial x} + \frac{R}{2}\frac{\partial V}{\partial x} = 0, \tag{5.5}$$

and conservation of momentum equals

$$\frac{\partial V}{\partial t} + (2\alpha - 1)\,V\frac{\partial V}{\partial x} + 2\,(\alpha-1)\frac{V^2}{R}\frac{\partial R}{\partial x} + \frac{1}{\rho}\frac{\partial p}{\partial x} = -2\frac{\nu\alpha}{\alpha-1}\frac{V}{R^2} \tag{5.6}$$

(see Smith *et al.* (2002) for details). Equations (5.5) and (5.6) provide two equations in the three unknowns, (V, p, R). A third constitutive equation which describes the relationship between pressure and radius, R, must be established. Ignoring any transient or visco-elastic properties of the vessel wall, an empirical relationship between transmural pressure and the radius can be established, which is of the form

$$p(R) = G_o\left[\left(\frac{R}{R_o}\right)^{\beta} - 1\right]. \tag{5.7}$$

The form of equation (5.7) was chosen to provide a good fit to experimental pressure–radius data. The solution to equations (5.5)–(5.7) characterizes transient blood flow in the coronary network.

5.2. Branching in vessel networks

Equations governing fluid flow at bifurcations within a network must now be introduced in order to model blood flow through branching structures such as the coronary network. The bifurcation model is based around an approximation of the junction between vessels as three short elastic tubes of radius R_a, R_b and R_c, respectively. If the tubes are assumed to be sufficiently short then the velocity along them is constant, *i.e.*, they are parallel-sided and losses due to fluid viscosity are negligible. Furthermore, no fluid is assumed to be stored within the junction. The location of the parent vessel entering the junction is denoted by a and the points at the beginning of the daughter vessels are labelled as b and c. If F_a, F_b and F_c are the rates of flow through each junction segment and P_o is the pressure at the junction centre, then conservation of mass through the junction is governed by

$$F_a - F_b - F_c = 0. \tag{5.8}$$

The conservation of momentum for tube a is governed by the resultant axial force equalling the rate of change of momentum of fluid in a segment length l_a of radius R_a, *i.e.*,

$$R_a^2(p_a - p_b) = \rho\left(\frac{\partial(l_a R_a^2 V_a)}{\partial t} + \frac{\partial(l_b R_b^2 V_b)}{\partial t}\right), \tag{5.9}$$

along with similar expressions for the flows between tubes a and c, and tubes b and c. Having introduced equations (5.8) and (5.9), which govern the conservation of mass and momentum across the bifurcation, the next step is to couple these to the single vessel equations (5.5)–(5.7). This is achieved by manipulating the pressures at the three segment ends that form a bifurcation such that the flows F_a, F_b and F_c simultaneously satisfy equations (5.8) and (5.9). This manipulation can be cast as a root-finding problem. The boundary conditions from the single vessel elements are used to calculate flows in each segment for a given pressure and partial derivatives of flow with respect to pressure $\frac{\partial F}{\partial p}$. From these equations a Newton–Raphson step can be calculated to determine the change in the pressure increments in tubes a, b and c required to satisfy equations (5.8) and (5.9) to linear order. To account for the nonlinearities this calculation is iterated using the new pressure values until the solution converges.

5.3. Microcirculation

The microcirculation network is formed by the terminal branching arterial and venous networks, called arterioles and venules, and the capillaries that connect them. This network is both topologically and functionally different from the network of large-conduit vessels. These vessels have diameters

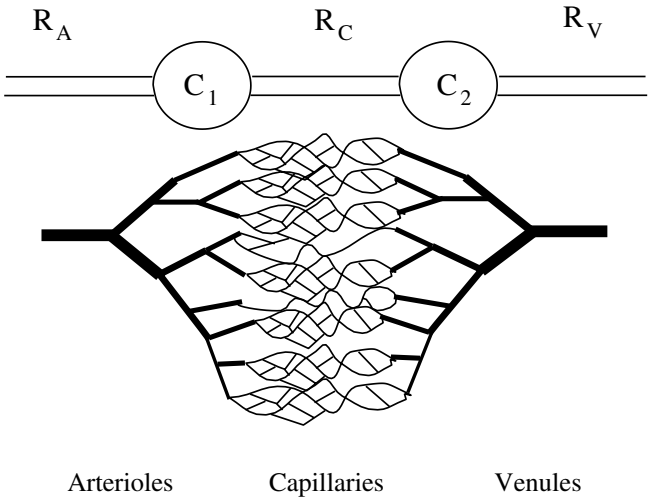

Figure 5.1. Schematic of the lumped parameter microcirculation model with the lumped comments for volume capacitance and resistance to flow shown.

comparable to the size of a red blood cell. At this spatial scale blood can no longer be considered as a homogeneous Newtonian fluid and the flow properties are strongly influenced by the individual red blood cells (Pries, Neuhaus and Gaehtgens 1992). This affects fluid viscosity (known as the Fahraeus effect), flow profiles and distribution of flow at bifurcations (Pries, Ley, Claasen and Gaehtgens 1989). Thus the equations used to model flow through the larger vessels in this study are no longer valid. The large number of microcirculation networks connecting each arteriole to a venule also makes the method of discretely modelling individual vessel segments for each microcirculation network computationally prohibitive. To overcome these problems a lumped parameter model of microcirculation has been developed based on the intramyocardial pump of Spaan, Breuls and Laird (1981). This model is used to reproduce the observed flow responses to arteriole and venule pressure of an anatomically based model combining nonlinear resistive and capacitive elements, reproducing experimentally observed behaviour in a computationally efficient way, while retaining some of the fundamental physics of the problem. A five-element lumped parameter model is shown schematically in Figure 5.1. R_A, R_C and R_V are arterial, capillary and venule resistances, respectively, and C_1 and C_2 represent the proximal and distal capacitances of the microcirculation model. The rate of change of pressure is related to the net flow across the capacitive

components, and hence the pressure drop, according to

$$C_1 \frac{\mathrm{d}p_1}{\mathrm{d}t} = F_A - F_C = \frac{P_A - P_1}{R_A} - \frac{P_1 - P_2}{R_C}, \tag{5.10}$$

$$C_2 \frac{\mathrm{d}p_2}{\mathrm{d}t} = F_C - F_V = \frac{P_1 - P_2}{R_C} - \frac{P_2 - P_V}{R_V}. \tag{5.11}$$

These equations are then coupled to the terminal segment end of the arteriole and venule models using the same root-find techniques employed to determine bifurcation flows. The Newton–Raphson method is used to iteratively converge to the P_A and P_V pressure values that, via single segment boundary condition, give flows F_A and F_V.

5.4. Coupled blood flow and tissue mechanics

The effect of contraction of the heart and skeletal muscles around the embedded vessels is an important determinant of blood flow (Downey and Kirk 1975, Spaan *et al.* 1981, Krams, Sipkema and Westerhof 1989). There are two distinct steps to coupling coronary blood flow to the pressure exerted by the other host organ on the embedded vessels, firstly calculation of the pressure exerted on the vessel wall and secondly to include this pressure in the blood flow models presented above.

For each vessel, the pressure exerted on the vessel wall as a function of time and distance along the vessel must be calculated. The pressure acting on a vessel wall at a given point along the length of a vessel is assumed to be the average of the radial forces acting normal to the wall. The starting point in determining this pressure is the second Piola–Kirchoff stress tensor $T^{\alpha\beta}$, calculated by solving the finite deformation equations which govern the deformation of the host medium (Section 3.1). This stress tensor is defined in the local material coordinates (ν_1, ν_2, ν_3) (see Figure 5.2).

$T^{\alpha\beta}$ does not directly provide information about the physical stresses. The objective is to use the second Piola–Kirchoff stress tensor to determine the Cauchy stress tensor σ^{ij} in a deformed rectangular Cartesian coordinate system. Using σ^{ij} the physical stresses can then be calculated. The Cauchy stress tensor is related to the 2nd Piola–Kirchoff stress tensor in this Cartesian coordinate system (Malvern 1969) by the following relation:

$$\sigma^{(x)} = \frac{1}{J} \boldsymbol{F} T^{(\nu)} \boldsymbol{F}^{\boldsymbol{T}}. \tag{5.12}$$

F is evaluated using the material coordinates of the host finite element mesh ξ and the reference coordinate system of that host mesh θ:

$$\frac{\partial x_i}{\partial \nu_M} = \frac{\partial x_i}{\partial \theta_j} \frac{\partial \theta_j}{\partial \xi_k} \frac{\partial \xi_k}{\partial \nu_M}. \tag{5.13}$$

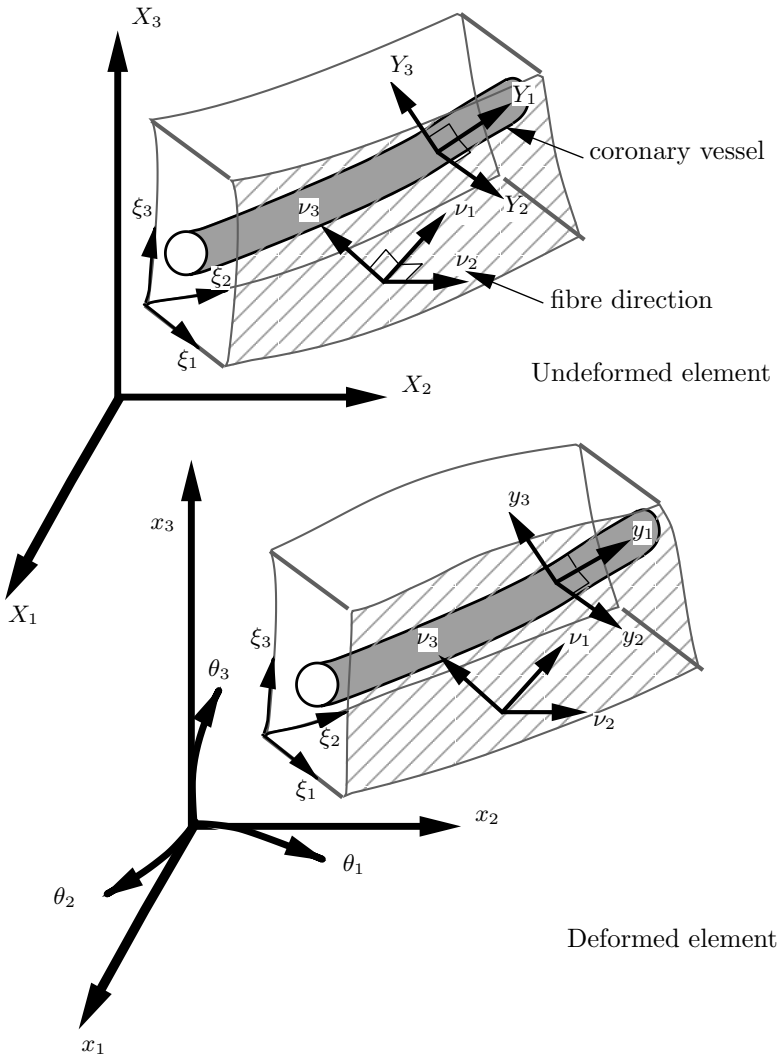

Figure 5.2. Coordinate systems used in the kinematic analysis of large-deformation finite element host mesh with embedded coronary elements. The axes (X_1, X_2, X_3) are the material Cartesian coordinates aligned with the reference coordinates (x_1, x_2, x_3) in the undeformed state. (ν_1, ν_2, ν_3) are the material coordinates aligned with the tissue microstructure; these are defined to be orthogonal in the undeformed state. (ξ_1, ξ_2, ξ_3) are the local finite element material coordinates. (Y_1, Y_2, Y_3) and (y_1, y_2, y_3) are the Cartesian set of coordinates which are orthogonal and aligned with the vessel direction in the undeformed and deformed states respectively. $(\theta_1, \theta_2, \theta_3)$ are the curvilinear reference coordinate system.

To evaluate the stresses on the vessel wall the Cauchy stress tensor is transformed into a rectangular Cartesian coordinate system y in which the local deformed vessel geometry is referenced:

$$\sigma^{ij(y)} = \frac{\partial y_i}{\partial x_k}\sigma^{kl(x)}\frac{\partial y_j}{\partial x_l}. \tag{5.14}$$

According to Cauchy's formula, the stress vector in Cartesian coordinates $\boldsymbol{t}$ (the force per unit area acting on a surface with unit normal $\boldsymbol{n}$) is given by (Spencer 1980)

$$\boldsymbol{t} = \sigma^{ij} n_i \boldsymbol{g_j}, \tag{5.15}$$

where $\boldsymbol{g_j}$ are the base vectors of the coordinate system. From this expression, the normal stress, t_n, acting perpendicular to a surface with a normal n_i is

$$t_n = \sigma^{ij} n_i n_j. \tag{5.16}$$

By determining a vector normal to the vessel wall the normal stress acting on the wall can therefore be calculated. This can be further simplified by aligning y_1 in the direction of the vessel, y_2 normal to y_1 and to the x axis and choosing y_3 as the cross-product of y_1 and y_2. Thus both y_2 and y_3 are normal to the vessel axis. The average normal stress in the radial direction is then

$$t_{\text{wall}} = \frac{1}{2}(\sigma^{22(y)} + \sigma^{33(y)}) \tag{5.17}$$

and t_{wall} is taken as the stress acting on the vessel wall.

Once the pressures are determined the second step is to include the reaction of the vessel wall to the varying pressure and deformation in the blood flow model presented in Section 5.1. Deformation of the host organ finite element mesh produces deformation of the embedded vessel geometry. This deformation is calculated by using one set of ξ positions within the mesh geometry to fix vessel segments at material points inside the mesh. As the mesh deforms the position of the vessels is calculated by reinterpolating the basis functions using the deformed geometry at the fixed ξ positions. Using this method axial vessel strain (denoted by λ) can be determined from the solution of the finite deformation equations (an example of the calculated deformation of embedded vessels is shown in Figure 5.3).

The elastic pressure–radius relationship must be modified such that pressure within a vessel is the sum of two terms: the reaction of the fluid on the elastic vessel wall and the pressure

$$P(R) = G_o\left[\left(\frac{R\sqrt{\frac{\lambda}{\lambda_o^*}}}{R_o^*}\right)^{\beta_1\lambda+\beta_2} - 1\right] - t_{\text{wall}}, \tag{5.18}$$

exerted on the wall by the deforming host medium, where β_1,β_2 and G_o are empirical parameters fitted from experimental data.

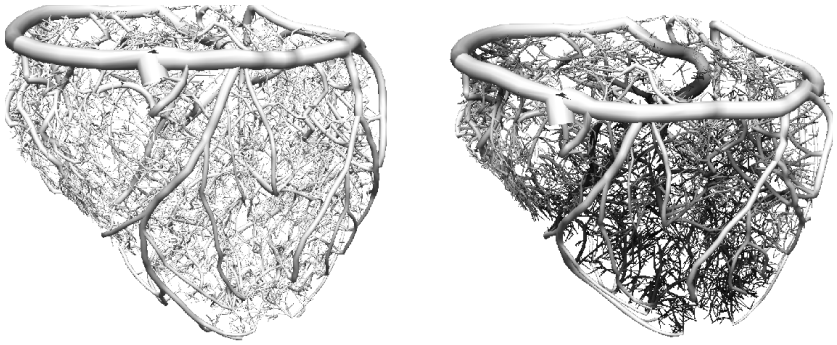

(a) (b)

Figure 5.3. A coupled model of coronary arterial blood flow and myocardial mechanics showing calculated intramyocardial pressure mapped on to the deformed coronary arterial geometry at two stages of the heart cycle: (a) start of contraction and (b) end of contraction. Shading indicates the degree of pressure exerted on the vessels by contraction.

To account for deformation, *i.e.*, stretch or compression of vessels, the conservation equations for mass and momentum are also modified:

$$\frac{\partial\left(R\sqrt{\lambda}\right)}{\partial t} + \frac{R\sqrt{\lambda}}{2}\frac{\partial V}{\partial x} + V\sqrt{\lambda}\frac{\partial R}{\partial x} = 0, \tag{5.19}$$

$$\frac{\partial V}{\partial t} + (2\alpha - 1)V\frac{\partial V}{\partial x} + 2(\alpha - 1)\frac{V^2}{R}\frac{\partial R}{\partial x} + \frac{1}{\rho}\frac{\partial p}{\partial x} = \frac{-\alpha\nu SV(a^2 + b^2)}{(\alpha - 1)\pi a^3 b^3}. \tag{5.20}$$

The solution techniques for these modified blood flow equations are unchanged. However, the λ and t_{wall} values vary with time and thus require updating at each time-step. This can be achieved via linear interpolation of values calculated from mechanics solutions which are usually incremented with a significantly greater time-step than that used in the flow solution.

Numerical and computational issues

Calculations of coronary blood flow for the whole heart are computationally intensive owing to the large number of finite difference grid points and the number of network bifurcations and lumped parameter microcirculation models to be solved at terminal branching of the network. The computational storage required for the implementation of an implicit method is prohibitive. The explicit two-step Lax–Wendroff finite difference scheme is a suitable solution method for the set of equations which is second-order

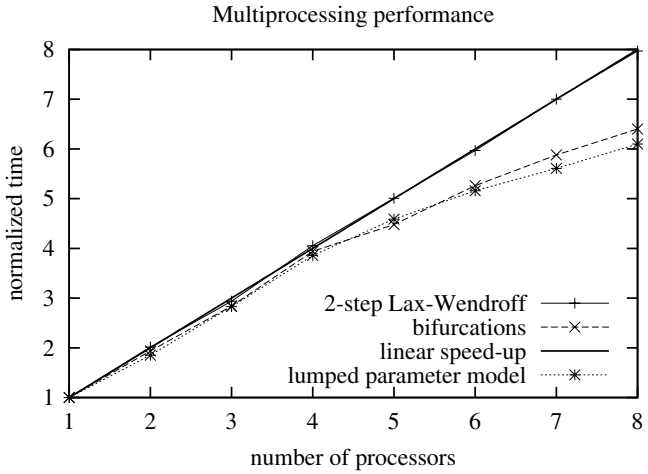

Figure 5.4. The normalized time $\frac{T_1}{T_n}$, where T_1 is the time taken using one processor and T_n is the time taken using n processors, as a function of number of processors n for 10000 time-steps solving for flow variables on the first three generations of the full coronary mesh.

accurate in both time and space, and also eliminates large numerical dissipation (Press, Teukolsky, Vetterling and Flannery 1992). For a detailed analysis of the stability properties of this approach see Smith *et al.* (2002).

A major advantage of the explicit Lax–Wendroff scheme, applied to the blood flow equations, is the ability to divide the computational effort at a given time-step evenly between processors with little additional work. The scalability is demonstrated in Figure 5.4 for a typical network simulation on a shared memory Silicon Graphics Power Challenge. The computation times for the finite difference calculations are very close to the theoretical ideal of linear speed-up, indicating an efficient parallelization, in this case using simple scheduling to divide grid points evenly between processors. The computation times for the network elements, both for bifurcations and microcirculation calculations, do not show linear speed-up. More iterations are needed to reach convergence in regions of the coronary network where large pressure gradients occur. Thus, to avoid computational bottlenecks, where a large subset of the processors may be idle, dynamic scheduling can be used to divide computational work between processors. The computational overhead, however, increases and efficiency drops as the number of processors is increased, as shown in Figure 5.4 by the fall away from the ideal linear speed-up.

6. Future directions

Having presented a framework for integrative modelling linking across multiple physical processes at one spatial scale (mechanics, electrical wave propagation and coronary blood flow) and across multiple spatial scales (subcellular, ion channels to the intact organ), we now explore future directions for this work and present models from two other organ systems developed using this framework.

6.1. Multiscale modelling in the heart

The framework for computational physiology presented here, and illustrated in relation to the heart, requires anatomically and biophysically based models to be developed at multiple spatial scales from genes to the intact organism.

At the organ level the models are based on physical conservation laws and are solved with numerical techniques that are typically finite element or boundary element methods, since these are readily able to cope with the complex three-dimensional geometries. A feature of the models at this level is that they must deal with more than one type of physical problem. Large deformation mechanics in the heart, for example, is solved with Galerkin finite element techniques coupled closely with the solution of the reaction–diffusion equations governing electric current flow around the heart. This latter technique uses a computational grid which is tied to material points of the moving finite element mesh, but the spatial resolution requirements for these two processes are quite different. Spatial convergence for the mechanics is achieved with a finite element mesh of around 100 tricubic-Hermite elements but convergence for the reaction–diffusion equations requires a mesh resolution of 0.1–0.2 mm, corresponding to 30 million grid points if implemented for the whole heart. The challenge now is to develop adaptive meshing techniques (multigrid, for example) which use the finely resolved meshes only in the vicinity of the moving wavefronts.

Another priority for model development at the organ level is to incorporate the measured spatial distribution of material parameters, such as the density variation of various ion channels in the heart (Akar and Rosenbaum 2003).

The organ systems for which models are currently at an advanced stage of development are the heart and circulation, the lungs, the musculo-skeletal system and the digestive system. The next-highest priorities are probably the kidney, endocrine pancreas and liver.

Tissue properties are included in the conservation laws of continuum mechanics (equations (3.10) and (3.5)) or electrophysiology (equations (3.14) and (3.15)) via material constitutive laws that express stress–strain relations (equation (3.12)) or current–voltage relations (equation (4.10)). The

next challenge at the tissue level is to relate these macroscopic continuum descriptions to detailed structural models of the tissue. Linking the parameters of these constitutive laws to the underlying tissue structure requires tissue models at the millimetre scale which include the distributions of type, orientation, density and cross-linking for collagen, proteoglycans and other extracellular matrix components. The properties of these tissue types must be linked to cellular properties within appropriate cell types. Similarly, the cellular processes such as ion transport, signal transduction, metabolic pathways, *etc.*, must be linked to the spatial distribution of proteins within cells and their enzyme and substrate-dependent binding reactions. In some cases these must also account for the reaction–diffusion behaviour of intracellular messengers.

Another important goal in multiscale heart modelling is the development of a three-dimensional (3D) myocyte cell model which can link the function of individual proteins to the integrated function of cells operating within the extracellular matrix (ECM). The forces developed by myofilaments during active contraction are conveyed to adjacent cells via intercellular gap junctions (formed from the protein connexin) and the surrounding ECM of collagen (the primary structural protein) and proteoglycans (with their electrically charged water binding groups). The internal structure of the myocytes is maintained by a network of intermediate filaments (primarily the protein desmin) (Balogh *et al.* 2002). Three-dimensional models that incorporate the spatial distribution and material properties of these ECM and intracellular structural proteins are needed. The 3D models also need to include the reaction–diffusion kinetics of mobile ions like H^+ and Ca^{2+} and the spatially localized action of signal transduction pathways.

6.2. Markup languages and ontologies

Mathematical modelling of physiological function at the level of tissues and cells often requires that independently developed models be combined. Signalling pathways within cells, for example, are highly interdependent and cannot be treated in isolation. This raises two very important issues for biological modellers. The first is the need for a standard format (a 'markup language') for encoding models in a robust, parsible, electronic form. Fortunately the recent development of XML[1] standards provides a platform for the development of modelling standards such as CellML (`www.cellml.org`) and SBML (`www.sbml.org`). The second is the need for consistent names for all the biological components (an 'ontology') and a strong typing con-

[1] eXtensible Markup Languages developed by the W3C (Worldwide web consortium `www.w3c.org`)

vention so that a particular protein such as PKA, for example, is labelled as a kinase (a type of enzyme) that can participate in a particular type of reaction (phosphorylation of a binding site on the target protein). This second requirement is being addressed by a number of international consortiums such as TAMBIS (`imgproj.cs.man.ac.uk/tambis`) and BioPAX (`www.biopax.org`).

6.3. Other organ systems

There are twelve organ systems in the body[2] and each component of these organ systems involves one or more of the four basic tissue types[3] which contain, depending on their location, a fraction of the approximately 200 different cell types. Here we briefly describe progress on applying the computational framework described above to two other organ systems.

The lungs

The dominant physical processes occurring at the organ level in the lungs are gas transport through the airways, blood flow in the pulmonary circulation and large-deformation mechanics of the soft parenchymal tissue. The airways are divided, on average, into 16 generations of conducting airways, which occupy about 150 ml of the 4 litre total air capacity, and 9 (on average) generations of respiratory airways in which gas exchange with the blood flow takes place. A finite element model of the conducting airways, based on CT data is shown in Figure 6.1 (Tawhai, Pullan and Hunter 2000). This model has been used to study gas transport (Tawhai and Hunter 2001*a*, 2001*b*) and the transport of heat and humidity in the conducting airways (Tawhai, Rankin, Ryan and Hunter 2002, Tawhai and Hunter 2004).

The challenge now is to develop tissue models that incorporate the structure and functional properties of the epithelial and connective tissue surrounding the airways and pulmonary blood vessels. Once the three major physical processes dominating lung function (air flow, blood flow and tissue mechanics) have been modelled, the spatial distribution of cell types can be included and the link made to diseases of the lungs such as COPD (chronic obstructive pulmonary disease) and asthma.

The musculo-skeletal system

Anatomically based models from the musculo-skeletal system are shown in Figure 6.2. This includes tricubic-Hermite models of bones and muscle

[2] Cardiovascular system, respiratory system, muscular-skeletal system, skin (integument), digestive system, urinary system, nervous system, endocrine system, lymphoid system, male reproductive system, female reproductive system and the special sense organs.

[3] Connective tissue, epithelial tissue, muscle tissue and nervous tissue.

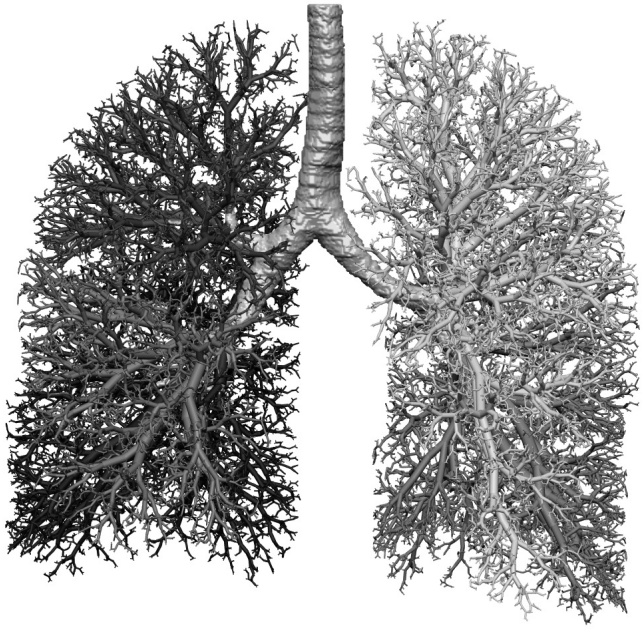

Figure 6.1. A model of the human airways for studying gas transport and exchange in the lungs. From Crampin *et al.* (2004), with permission

(a) Three-dimensional bone structure.

(b) The fitted femur bone model.

(c) Finite element models of the muscles and tendons of the human forearm.

Figure 6.2. Examples of images and finite element models from the musculo-skeletal system.

which incorporate the underlying microstructure using the method previously applied to the heart. For certain regions of the body, such as the legs, the fibrous structure of the muscles has also been fitted to experimental data and the tendons, ligaments and cartilage are also included. One current application is examining the distribution of stress over the head of the femur as the patella (knee cap) rolls over it. Note that the geometric fitting processes used here are very similar to those described in Section 2.2 for the heart and the equations governing mechanics are also similar to those described in Section 3.1. Bone, which is a linearly elastic compressible material, can be treated within the same nonlinear elasticity framework used for muscle, tendons and cartilage provided that the strain energy function equation (3.12) is spatially modified.

Again, the goal here is to link models of detailed structure (bone trabeculae and the soft connective tissues of skeletal muscle and cartilage) to continuum constitutive law parameters and then to incorporate the distribution of cell types and cell level processes to link the tissue and organ models to diseases such as osteoporosis and rheumatoid arthritis.

7. Conclusion

In this paper we have discussed computational modelling of organ systems (the heart in particular) at several spatial scales. At the level of the intact organ this requires the solution of partial differential equations expressing physical conservation laws, such as conservation of mass and momentum for mechanics and conservation of current for electrical activation.

The challenges from a numerical perspective are finding efficient ways of coupling the various physical systems (large-deformation mechanics, electrical wave propagation, fluid flow, *etc.*), each of which has its own characteristic length and time scales. Another challenge is linking across spatial scales from subcellular protein pathways to integrated cell function and then to tissue and organ behaviour. For electrical activation in the heart we have shown in this review how the solution of equations governing the electrophysiology of subcellular ion channels can be linked to the reaction–diffusion equations at the tissue and whole organ level.

The major challenges for the heart modelling work are: (i) to extend the organ level models to include other anatomical structures such as the atria and heart valves, (ii) to extend the tissue level models to incorporate more detail on extracellular matrix structure and how this changes in disease, and (iii) to extend cellular level models to incorporate signal transduction and metabolic pathways and how these are altered by disease.

The physiological accuracy of these continuum models depends critically on the constitutive laws (both the functional form and spatially varying parameter values) that define the relationships between stress and strain,

current and voltage gradient, *etc.* The fact that the constitutive law parameters do vary spatially is a reflection of the inhomogeneous structure of the underlying tissue, which grows and remodels to suit its local functional requirements. Since it is generally not possible to measure experimentally the constitutive law parameters throughout an organ, an alternative approach is to establish a relationship between the constitutive law and the underlying microstructure of the tissue. Constitutive parameters can then be inferred from observations of structure throughout an organ. Establishing the relationship between microstructure and the continuum constitutive law requires micromechanical models which incorporate extracellular matrix structure as well as subcellular cytoskeletal structure. Such models are now under development.

Finally, the multi-physics and multiscale continuum modelling framework presented here is applicable across all organ systems and tissue types. Models of the lungs, musculo-skeletal system and digestive system are well under way.

Acknowledgements
The authors gratefully acknowledge many contributions by colleagues in the Auckland Bioengineering Institute. We are also grateful for the support of grants from the NZ Royal Society (to the Centre for Molecular Biodiscovery and the New Zealand Institute of Mathematics and its Applications) and the NZ Foundation for Research Science and Technology.

REFERENCES

M. J. Ackerman (1998), 'The Visible Human project', *Proc. IEEE* **86**, 504–511.

F. G. Akar and D. S. Rosenbaum (2003), 'Transmural electrophysiological heterogeneities underlying arrhythmogenesis in heart failure', *Circ. Res.* **93**, 638–645.

R. J. Atkin and N. Fox (1980), *An Introduction to the Theory of Elasticity*, Longman, London.

J. Balogh, M. Merisckay, Z. Li, D. Paulin and A. Arner (2002), 'Hearts from mice lacking desmin have a myopathy with impaired active force generation and unaltered wall compliance', *Cardiovasc. Res.* **53**, 439–450.

D. A. Bergel and P. J. Hunter (1979), The mechanics of the heart, in *Quantitative Cardiovascular Studies, Clinical and Research Applications of Engineering Principles* (N. H. C. Hwang, D. R. Gross and D. J. Patel, eds), University Park Press, Baltimore, chapter 4, pp. 151–213.

C. P. Bradley, A. J. Pullan and P. J. Hunter (1997), 'Geometric modelling of the human torso using cubic Hermite elements', *Ann. Biomed. Eng.* **76**, 96–111.

M. Buist, G. B. Sands, P. J. Hunter and A. J. Pullan (2003), 'A deformable finite element derived finite difference method for cardiac activation problems', *Ann. Biomed. Eng.* **31**, 577–588.

Y. I. Cho and R. Kensey (1991), 'Effects of the non-Newtonian viscosity of blood flows in a diseased arterial vessel', *Biorheology* **28**, 241–262.

K. D. Costa, P. J. Hunter, J. M. Rogers, J. M. Guccione, L. K. Waldman and A. D. McCulloch (1996*a*), 'A three-dimensional finite element method for large elastic deformations of ventricular myocardium, Part I: Cylindrical and spherical polar coordinates', *ASME J. Biomech. Eng.* **118**, 452–463.

K. D. Costa, P. J. Hunter, J. S. Wayne, L. K. Waldman, J. M. Guccione and A. D. McCulloch (1996*b*), 'A three-dimensional finite element method for large elastic deformations of ventricular myocardium, Part II, Prolate spheroidal coordinates', *ASME J. Biomech. Eng.* **118**, 464–472.

E. J. Crampin, M. Halstead, P. J. Hunter, P. Nielsen, D. Noble, N. Smith and M. Tawhai (2004), 'Computational physiology and the Physiome project', *Exp. Physiol.* **89**, 1–26.

J. Demmel, S. Eisenstat, J. Gilbert, X. Li and J. Liu (1999*a*), 'A supernodal approach to sparse partial pivoting', *SIAM J. Mat. Anal. Appl.* **20**, 720–755.

J. Demmel, J. Gilbert and X. Li (1999*b*), 'An asynchronous parallel supernodal algorithm for sparse Gaussian elimination', *SIAM J. Mat. Anal. Appl.* **20**, 915–952.

D. DiFrancesco and D. Noble (1985), 'A model of cardiac electrical activity incorporating ionic pumps and concentration changes', *Phil. Trans. R. Soc. Lond. B* **307**, 353–398.

J. M. Downey and E. S. Kirk (1975), 'Inhibition of coronary blood flow by a vascular waterfall mechanism', *Circ. Res.* **36**, 753–760.

J. L. Emery, J. H. Omens and A. D. McCulloch (1997), 'Biaxial mechanics of the passively overstretched left ventricle', *Amer. J. Physiol.* **272**, H2299–H2305.

G. Fischer, B. Tilg, R. Modre, G. J. M. Huiskamp, J. Fetzer, W. Rucker and P. Wach (2000), 'A bidomain model based BEM-FEM coupling formulation for anisotropic cardiac tissue', *Ann. Biomed. Eng.* **28**, 1229–1243.

J. L. Greenstein and R. L. Winslow (2002), 'An integrative model of the cardiac ventricular myocyte incorporating local control of ca2+ release', *Biophys. J.* **83**, 2918–2945.

J. M. Guccione, A. D. McCulloch and L. K. Waldman (1991), 'Passive material properties of intact ventricular myocardium determined from a cylindrical model', *ASME J. Biomech. Eng.* **113**, 42–55.

J. M. Guccione, I. Motabarzadeh and G. I. Zahalak (1998), 'A distribution-moment model of deactivation in cardiac muscle', *J. Biomech.* **31**, 1069–73.

A. Guz, D. H. Bergel and D. L. Brutsaert (1974), *The Physiological Basis of Starling's Law of the Heart*, Elsevier.

C. S. Henriquez (1993), 'Simulating the electrical behaviour of cardiac tissue using the bidomain model', *Crit. Rev. Biomed. Eng.* **21**, 1–77.

T. L. Hill (1975), 'Theoretical formalism for the sliding filament model of contraction of striated muscle, part II', *Prog. Biophys. Molec. Biol.* **29**, 105–159.

T. L. Hill (1989), *Free Energy Transduction and Biochemical Cycle Kinetics*, Springer, New York.

A. C. Hindmarsh (1983), ODEPACK, a systematized collection of ode solvers, in *Scientific Computing* (R. S. Stepleman, ed.), North-Holland, Amsterdam, pp. 55–64.

A. L. Hodgkin (1976), 'Chance and design in electrophysiology: An informal account of certain experiments on nerve carried out between 1934 and 1952', *J. Physiol.* (*Lond.*) **263**, 1–21.

A. L. Hodgkin and A. F. Huxley (1952), 'A quantitative description of membrane current and its application to conduction and excitation in nerve', *J. Physiol.* (*Lond.*) **117**, 500–544.

P. J. Hunter (1975), Finite element analysis of cardiac muscle mechanics, DPhil thesis, University of Oxford.

P. J. Hunter (1995), Myocardial constitutive laws for continuum mechanics models of the heart, in *Molecular and Subcellular Cardiology: Effects of Structure and Function* (S. Sideman and R. Beyar, eds), Plenum Press, chapter 30, pp. 303–318.

P. J. Hunter, A. D. McCulloch and H. E. D. J. ter Keurs (1998), 'Modelling the mechanical properties of cardiac muscle', *Prog. Biophys. Molec. Biol.* **69**, 289–331.

P. J. Hunter, M. P. Nash and G. B. Sands (1997), Computational electromechanics of the heart, in *Computational Biology of the Heart* (A. V. Panfilov and A. V. Holden, eds), Wiley, Chichester, chapter 12, pp. 345–407.

P. J. Hunter, B. H. Smaill and I. W. Hunter (1995), 'A 'pole-zero' constitutive law for myocardium', *ASME J. Biomech. Eng.* **382**, 303–18.

A. F. Huxley (1957), 'Muscle structure and theories of contraction', *Prog. Biophys. Chem.* **7**, 255–318.

S. Jafri, J. Rice and R. Winslow (1998), 'Cardiac Ca^{2+} dynamics: The role of ryanodine receptor adaptation and sarcoplasmic reticulum load', *Biophys. J.* **74**, 1149–1168.

B. Kantor, H. Kwon, E. Ritman, D. Holmes and R. Schwartz (1999), 'Images in cardiology imaging the coronary microcirculation: 3d Micro-CT of coronary vasa vasorum', *Internat. J. Cardiovasc. Intervent.* **2**, 79.

G. S. Kassab and Y. C. Fung (1994), 'Topology and dimensions of pig coronary capillary network', *Amer. J. Physiol.* **267**, H319–H325.

G. S. Kassab, C. A. Rider, N. J. Tang and Y. C. Fung (1993), 'Morphometry of pig coronary arterial trees', *Amer. J. Physiol.* **265**, H350–H365.

M. Kawai and W. P. Brandt (1980), 'Sinusoidal analysis: A high resolution method for correlating biochemical reactions with physiological processes in activated skeletal muscles of rabbit, frog and crayfish', *J. Mus. Res. Cell Motil.* **3**, 279–303.

M. Kawai, Y. Saeki and Y. Zhao (1993*a*), 'Crossbridge scheme and the kinetic constants of elementary steps deduced from chemically skinned papillary and trabecular muscles of the ferret', *Circ. Res.* **73**, 35–50.

M. Kawai, Y. Zhao and H. Halvorson (1993*b*), 'Elementary steps of contraction probed by sinusoidal analysis technique in rabbit psoas fibers', *Circ. Res.* **332**, 567–580.

J. Keener and J. Sneyd (1998), *Mathematical Physiology*, Springer, New York.

R. Krams, P. Sipkema and N. Westerhof (1989), 'Varying elastance concept may explain coronary systolic flow impediment', *Amer. J. Physiol.* **257**, H1471–H1479.

W. Krassowska and J. C. Neu (1994), 'Effective boundary conditions for syncytial tissues', *IEEE Trans. Biomed. Eng.* **41**, 143–150.

I. J. Le Grice, B. H. Smaill, L. Z. Chai, S. G. Edgar, J. B. Gavin and P. J. Hunter (1995), 'Laminar structure of the heart: Ventricular myocyte arrangement and connective tissue architecture in the dog', *Amer. J. Physiol.* **269**, H571–H582.

X. S. Li and J. W. Demmel (2003), 'SuperLU_DIST: A scalable distributed-memory sparse direct solver for unsymmetric linear systems', *ACM Trans. Math. Software* **29**, 110–140.

C.-H. Luo and Y. Rudy (1991), 'A model of the ventricular cardiac action potential: Depolarisation, repolarisation, and their interaction', *Circ. Res.* **68**, 1501–1526.

C.-H. Luo and Y. Rudy (1994), 'A dynamic model of the cardiac ventricular action potential, I: Simulations of ionic currents and concentration changes', *Circ. Res.* **74**, 1071–1096.

L. E. Malvern (1969), *Introduction to the Mechanics of a Continuous Medium*, Prentice-Hall, New Jersey.

S. F. McCormick (1989), *Multilevel Adaptive Methods for Partial Differential Equations*, SIAM.

R. M. Miura (2002), 'Analysis of excitable cell models', *J. Comput. Appl. Math.* **144**, 29–47.

A. L. Muzikant and C. S. Henriquez (1998), 'Bipolar stimulation of a three-dimensional bidomain incorporating rotational anisotropy', *IEEE Trans. Biomed. Eng.* **45**, 449–462.

M. P. Nash and P. J. Hunter (2000), 'Computational mechanics of the heart', *J. Elasticity* **61**, 112–141.

D. G. Nicholls and S. J. Ferguson (2002), *Bioenergetics 3*, Academic Press, London.

D. P. Nickerson, N. P. Smith and P. J. Hunter (2001), 'A model of cardiac cellular electromechanics', *Phil. Trans. R. Soc. Lond. A* **359**, 1159–1172.

P. M. F. Nielsen, I. J. Le Grice, B. H. Smaill and P. J. Hunter (1991), 'Mathematical model of geometry and fibrous structure of the heart', *Amer. J. Physiol.* **260**, H1365–H1378.

D. Noble (1960), 'Cardiac action and pacemaker potentials based on the Hodgkin–Huxley equations', *Nature* **188**, 495–497.

D. Noble, A. Varghese, P. Kohl and P. Noble (1998), 'Improved guinea-pig ventricular model incorporating diadic space, i_{kr} and i_{ks}, length and tension-dependent processes', *Canad. J. Cardiol.* **14**, 123–134.

V. P. Novak, F. C. P. Yin and J. D. Humphrey (1994), 'Regional mechanical properties of passive myocardium', *J. Biomech.* **27**, 403–412.

J. T. Oden (1972), *Finite Elements of Nonlinear Continua*, McGraw-Hill, New York.

L. H. Opie (1998), *The Heart: Physiology, from Cell to Circulation*, 3rd edn, Lippincott-Raven.

K. Perktold, M. Resch and R. O. Peter (1991), 'Three-dimensional numerical analysis of the pulsatile flow and wall shear stress in the carotid artery bifurcation', *J. Biomech.* **24**, 409–420.

G. Piazzesi and V. Lombardi (1995), 'A cross-bridge model that is able to explain mechanical and energetic properties of shortening muscle', *Biophys. J.* **68**, 1966–1979.

R. Plonsey and R. C. Barr (1984), 'Current flow patterns in two-dimensional anisotropic bisyncytia with normal and extreme conductivities', *Biophys. J.* **45**, 557–571.

W. H. Press, S. A. Teukolsky, W. T. Vetterling and B. P. Flannery (1992), *Numerical Recipes in FORTRAN: The Art of Scientific Computing*, 2nd edn, Cambridge University Press, Cambridge.

A. R. Pries, K. Ley, M. Claasen and P. Gaehtgens (1989), 'Red cell distribution at microvascular bifurcations', *Microvasc. Res.* **38**, 81–101.

A. R. Pries, D. Neuhaus and P. Gaehtgens (1992), 'Blood viscosity in tube flow: Dependence on diameter and hematocrit', *Amer. J. Physiol.* **263**, H1770–H1778.

J. J. Rice and P. P. de Tombe (2004), 'Approaches to modeling crossbridges and calcium-dependent activation in cardiac muscle', *Prog. Biophys. Mol. Biol.*, DOI 10.1016/j.pbiomolbio.2004.01.011. In press.

B. J. Roth (1997), 'Electrical conductivity values used with the bidomain model of cardiac tissue', *IEEE Trans. Biomed. Eng.* **44**, 326–328.

B. J. Roth and J. P. Wikswo, Jr. (1986), 'A bidomain model for the extracellular potential and magnetic field of cardiac tissue', *IEEE Trans. Biomed. Eng.* **33**, 467–469.

S. Rusinkiewicz and M. Levoy (2001), 'Efficient variants of the icp algorithm', *Third International Conference on 3D Digital Imaging and Modeling* (*3DIM 2001 Proceedings*), pp. 145–152.

Y. Saeki, M. Kawai and Y. Zhao (1991), 'Comparison of crossbridge dynamics between intact and skinned myocardium from ferret right ventricles', *Circ. Res.* **68**, 772–81.

O. H. Schmitt (1969), Biological information processing using the concept of interpenetrating domains, in *Information Processing in the Nervous System* (K. N. Leibovic, ed.), Springer, New York, pp. 325–331.

K. B. Skouibine, N. A. Trayanova and P. K. Moore (2000), 'A numerically efficient model for simulation of defibrillation in an active bidomain sheet of myocardium', *Math. Biosci.* **166**, 85–100.

D. A. Smith (1998), 'A strain-dependent ratchet model of [phosphate]- and [atp]-dependent muscle contraction', *J. Mus. Res. Cell Motil.* **19**, 189–211.

N. P. Smith (2003), 'From sarcomere to cell: An efficient algorithm for linking mathematical models of muscle contraction', *Bull. Math. Biol.* **65**, 1141–1162.

N. P. Smith and E. J. Crampin (2004), 'Development of models of active ion transport for whole-cell modelling: Cardiac sodium–potassium pump as a case study', *Prog. Biophys. Molec. Biol.*, DOI 10.1016/j.pbiomolbio.2004.01.010. In press.

N. P. Smith, A. J. Pullan and P. J. Hunter (2000), 'The generation of an anatomically accurate geometric coronary model', *Ann. Biomed. Eng.* **28**, 14–25.

N. P. Smith, A. J. Pullan and P. J. Hunter (2002), 'An efficient finite difference model of transient coronary blood flow in the heart', *SIAM J. Appl. Math.* **62**, 990–1018.

J. A. E. Spaan, N. P. W. Breuls and J. D. Laird (1981), 'Diastolic -systolic coronary flow differences are caused by intramyocardial pump action in the anesthetised dog', *Circ. Res.* **49**, 584–593.

A. J. M. Spencer (1980), *Continuum Mechanics*, Longman, London.

M. Tawhai and P. J. Hunter (2001*a*), 'Characterising respiratory airway gas mixing using a lumped parameter model of the pulmonary acinus', *Respir. Physiol.* **127**, 241–248.

M. Tawhai and P. J. Hunter (2001*b*), 'Multibreath washout analysis: Modelling the influence of conducting airway asymmetry', *Respir. Physiol.* **127**, 249–258.

M. Tawhai and P. J. Hunter (2004), 'Modeling water vapour and heat transfer in the normal and the intubated airway', *Ann. Biomed. Eng.* In press.

M. H. Tawhai, A. J. Pullan and P. J. Hunter (2000), 'Generation of an anatomically based three-dimensional model of the conducting airways', *Ann. Biomed. Eng.* **28**, 793–802.

M. Tawhai, N. Rankin, S. Ryan and P. J. Hunter (2002), 'Measurement and mathematical modelling of thermodynamics within the intubated airway', *Eur. Respir. J.* **20**, 602s.

N. A. Trayanova (1994), 'A bidomain model for ring stimulation of a cardiac strand', *IEEE Trans. Biomed. Eng.* **41**, 393–397.

L. Tung (1978), A bidomain model for describing ischemic myocardial D-C potentials, PhD thesis, MIT, Boston, MA.

T. P. Usyk, I. J. Le Grice and A. D. McCulloch (2002), 'Computational model of three-dimensional cardiac electromechanics', *Comput. Visual Sci.* **4**, 249–257.

T. P. Usyk, R. Mazhari and A. D. McCulloch (2000), 'Effect of laminar orthotropic myofiber architecture on regional stress and strain in the canine left ventricle', *J. Elasticity* **61**, 143–164.

F. J. Vetter and A. D. McCulloch (2000), 'Three-dimensional stress and strain in passive rabbit left ventricle: A model study', *Ann. Biomed. Eng.* **28**, 781–92.

A. A. Young, Z. A. Fayad and L. Axel (1996), 'Right ventricular midwall surface motion and deformation using magnetic resonance tagging', *Amer. J. Physiol.* **271**, H2677–H2688.

A. A. Young, P. J. Hunter and B. H. Smaill (1989), 'Epicardial surface estimation from coronary cinéangiograms', *Comput. Vis. Graph. Image Proc.* **47**, 111–127.

G. I. Zahalak (1981), 'A distribution-moment approximation for kinetic theories of muscular contraction', *Mathematical Biosciences* **55**, 89–114.

G. I. Zahalak and S.-P. Ma (1990), 'Muscle activation and contraction: Constitutive relations based directly on cross-bridge kinetics', *ASME J. Biomech. Eng.* **112**, 52–62.

O. C. Zienkiewicz and R. L. Taylor (1994), *The Finite Element Method, I: Basic Formulation and Linear Problems*, 4th edn, McGraw-Hill, Berkshire.